Proceedings of Student Conference on Sensors, Systems and Measurement 2021

About the Conference

The conference was primarily intended for master's students and doctoral students of the Czech Technical University in Prague. Several presentations of the best bachelor's thesis results have been expected. However, students from domestic and foreign universities have also been more than welcomed.

The main topics of the conference will be Sensors, Measurements, Measuring Systems, Diagnostics and Testing divided into the following sections:

- Sensors, Materials and its Application
- Measurement of Electrical and Non-electrical Quantities
- Instrumentation and Measurement Systems
- Testing and Diagnostics
- Signal Processing
- System Identification and Control

The conference aimed to give students an opportunity to present their research results, improve their presentation skills, provide the floor for discussion, and exchange ideas and experience. Presentation of the best thesis results has raised awareness of topics solved at different laboratories and broadened the horizons for possible exchange and stays abroad.

Within the conference itself, lectures from the industrial area have been given to help students in deciding on their future professional life. Finally, yet importantly, it has been about the possibility of establishing cooperation between individual workplaces and industrial partners.

About the CTU in Prague

The Czech Technical University in Prague is the oldest technical University in the Czech Republic. Above all, our University forms the cornerstone of the Czech system for science & research. Our students can work on top research projects in collaboration with international teams and work closely with the University's industrial partners. The Faculties and Institutes of our University cover a broad spectrum of knowledge and capabilities, ranging from nuclear research to architecture, from artificial intelligence to healthcare, and from civil engineering to mechanical engineering. We offer educational and research capabilities in an extensive range of technical sciences, and we can satisfy almost every industrial demand for research or innovation.

Organizing Committee

- Ing. Jakub Svatoš, Ph.D. – Conference Chair
- Ing. Martin Šipoš, Ph.D. – Program Committee Chair
- prof. Ing. Pavel Ripka, CSc. – Technical Program Co-Chair
- Ing. Tomáš Drábek – Technical Program Co-Chair

Program Committee

- prof. Ing. Vladimír Haasz, CSc.
- prof. Ing. Jan Holub, Ph.D.
- Ing. Jan Plachý, Ph.D.
- Ing. Adam Bouřa, Ph.D.
- Ing. Tomáš Králík, Ph.D.
- Ing. Pavel Mužák
- Ing. Jan Vavrouš
- Ing. Ivo Trnka

Contact: scssm@fel.cvut.cz

ISBN 978-80-01-06822-9

Conference Programme

Monday, 14th June		
9:30 - 9:45	Start of the Conference	
	9:30 - 9:45	**Introduction of the Student Conference on Sensors, Systems and Measurement**
		Jan Holub, the Head of the Department of Measurement, Czech Technical University in Prague, Faculty of Electrical Engineering
10:00 - 11:30	Section A - Sensors, Materials and its Application I	
	10:00 - 10:15	**Industry partner I - Energomonitor**
		Full stack IoT development
	10:15 - 10:30	**Inkjet Printed Passive Components**
		Vojtěch Povolný, Czech Technical University in Prague, Faculty of Electrical Engineering
	10:30 - 10:45	**Simulation of Charge Diffusion and Fluorescent Photons in Pixelated CdTe Sensor**
		Jakub Jirsa, Czech Technical University in Prague, Faculty of Electrical Engineering
	10:45 - 11:00	**Cobalt Nanoparticles Anchored Nitrogen Doped Carbon Nanotubes for Highly Sensitive Sensing of Hydrogen Peroxide**
		Yue Hu, University of Science and Technology Beijing, School of Mathematics and Physics
	11:00 - 11:15	**Digital Guitar Pedal**
		Jakub Turinský, Czech Technical University in Prague, Faculty of Electrical Engineering
	11:15 - 11:30	**Possibilities of Using Magnetically Detectable Filament for The Magnetorquers Cores Production**
		Patrik Kašper, Technical University of Košice, Faculty of Aeronautics
13:00 - 14:30	Section B - Sensors, Materials and its Application II	
	13:00 - 13:15	**Industry partner II - Honeywell Aerospace - Advanced Technology Europe**
		The future is what we make it
	13:15 - 13:30	**Polymer Planar Bragg Gratings Based on Bulk Cyclic Olefin Copolymers: Fabrication and Functionalization**
		Stefan Kefer, TH Aschaffenburg, University of Applied Sciences
	13:30 - 13:45	**Parallel Fluxgate Sensor with Amorphous Wire Core: Sensitivity Study**
		Diana Hrakova, Czech Technical University in Prague, Faculty of Electrical Engineering
	13:45 - 14:00	**An Energy-efficient Self-oscillating Fluxgate Sensor for DC Current Measurement**
		Václav Grim, Czech Technical University in Prague, Faculty of Electrical Engineering
	14:00 - 14:15	**Simulation Model for a Low Cost Hts Squid System**
		Tessa Hall, Stellenbosch University, Stellenbosch, South Africa
	14:15 - 14:30	**Practical Aspects of an HTS SQUID Operating as a Geomegnetic Sensor**
		Elda F. Saunderson, SANSA Space Science, Hermanus, South Africa/Stellenbosch University, Stellenbosch, South Africa
	14:30 - 14:45	**Analysis of the Operator's Pilot Model when Controlling the UAV in the Longitudinal Plane**
		Šimon Karaffa, Technical University of Košice, Faculty of Aeronautics

Tuesday, 15th June		
9:00 - 10:15	Section C - Measurement of Electrical and Non-electrical Quantities	
	9:00 - 9:15	**Industry partner III - TMVSS**
		The goal of our company is to provide quality services to companies in the field of energy and industry
	9:15 - 9:30	**Software Defined Instrument Designed for Mass Distance Learning**
		Jakub Pařez, Czech Technical University in Prague, Faculty of Electrical Engineering
	9:30 - 9:45	**Radiation Testing of a Student-Designed Cubesat OBC**
		Filip Geib, Czech Technical University in Prague, Faculty of Electrical Engineering
	9:45 - 10:00	**A 1 ps Bin Size and 5.56 ps RMS Resolution FPGA Time-to-Digital Converter Based on Phase Wrapping, Sorting, and Selection**
		Joshua Adiel Wijaya, National Taiwan University of Science and Technology, Department of Electronic and Computer Engineeering
	10:00 - 10:15	**Hardware Platform for FRA and FDS Instrumentation**
		Jan Tomlain, Czech Technical University in Prague, Faculty of Electrical Engineering
	10:15 - 10:20	**iQNavs - indoor QR Navigation System**
		Martin Sipos, Czech Technical University in Prague, Faculty of Electrical Engineering
10:30 - 12:00	Section D - Signal Processing	
	10:30 - 10:45	**Industry partner IV - ESC Aerospace**
		The company focused on mission critical application, security and unmanned systems
	10:45 - 11:00	**Proton Magnetometer and Precession Signal Processing**
		Ondřej Bureš, Czech Technical University in Prague, Faculty of Electrical Engineering
	11:10 - 11:15	**Gunshot Detection and Classification**
		Michal Opočenský, Czech Technical University in Prague, Faculty of Electrical Engineering
	11:15 - 11:30	**DTW-Based Step Detection Algorithm for Pedestrian Dead Reckoning**
		Matěj Oravec, Czech Technical University in Prague, Faculty of Electrical Engineering
	11:30 - 11:45	**A High-performance FPGA Digital-to-Time Converter based on PLL Delay Matrix and Fine-Phase Shift Control**
		Joshua Adiel Wijaya, National Taiwan University of Science and Technology, Department of Electronic and Computer Engineeering
14:00	Awards, Closing of the Conference	

Content

Simulation of Charge Diffusion And Fluorescent Photons In Pixelated CdTe Sensor 7

Analysis of the Operator's Pilot Model When Controlling The UAV in the Longitudinal Plane 9

Polymer Planar Bragg Gratings Based on Bulk Cyclic Olefin Copolymers: Fabrication and Functionalization 11

Digital Guitar Pedal 13

Proton magnetometer and precession signal processing 15

Radiation Testing of a Student-Designed Cubesat OBC 17

An Energy-Efficient Self-Oscillating Fluxgate Sensor for DC Current Measurement 19

Simulation Model For a Low Cost HTS Squid System 21

Parallel Fluxgate Sensor with Amorphous Wire Core: Sensitivity Study 23

Cobalt Nanoparticles Anchored Nitrogen Doped Carbon Nanotubes for Highly Sensitive Sensing of Hydrogen Peroxide 25

Possibilities of Using Magnetically Detectable Filament for the Magnetorquers Cores Production 27

Gunshot Detection and Classification 29

DTW-Based Step Detection Algorithm for Pedestrian Dead Reckoning 31

Software Defined Instrument Designed for Mass Distance Learning 33

Inkjet Printed Passive Components 35

Practical Aspects of an HTS SQUID Operating as a Geomagnetic Sensor 37

Hardware Platform for FRA and FDS Instrumentation 39

SIMULATION OF CHARGE DIFFUSION AND FLUORESCENT PHOTONS IN PIXELATED CDTE SENSOR

Jirsa, J[1,2]
[1]Faculty of Electrical Engineering Czech Technical University in Prague, Czech Republic
[2]Faculty of Nuclear Sciences and Physical Engineering Czech Technical University in Prague, Czech Republic
jirsaja6@fel.cvut.cz

1. INTRODUCTION

Hybrid pixel detectors are becoming an integral part of medical imaging, material testing, space science, and many more. Hybrid pixel detectors consist of two parts: a chip with readout electronics and a bump bonded sensor with a top plated cathode and pixelated anode. Sensors are made from various materials such as Si, GeAs, and CdTe/CdZnTe. One of the commonly used materials for X-ray imaging is CdTe due to its high absorption efficiency in the X-ray spectrum. To increase the spatial resolution of the detectors, it is necessary to reduce the size of pixels. However, the decreasing size of pixel pitch leads to raising the impact of charge sharing and fluorescent photons. These effects cause that charge generated upon the absorption of gamma photon is registered by multiple pixels, leading to spectrum distortion. This study simulated the effect of charge sharing and fluorescent photons in 70 µm pixelated CdTe.

2. SENSOR SIMULATION

To simulate the effects of charge diffusion and fluorescent photons in CdTe, a 3D model of a 2 mm thick pixelated CdTe sensor was created. The sensor model is depicted in Figure 1. The sensor has a top-plated cathode and pixelated anode with a 5 x 5 pixel matrix with 70 µm pixel size. The sensor was biased at -1000 V. To simulate the sensor's spectral response, a photon beam with various photon energy was focused on the central pixel.

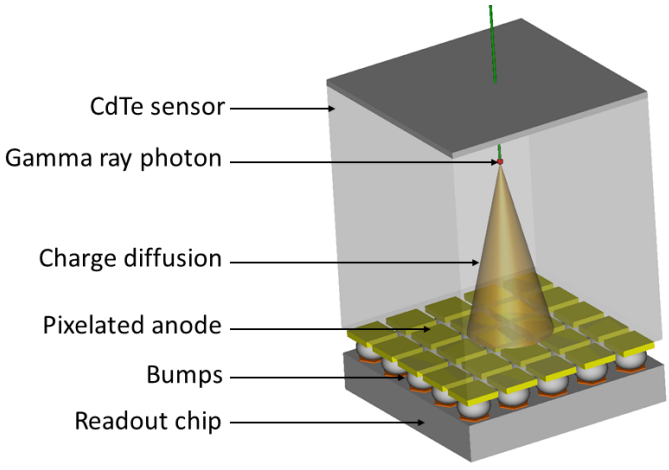

Figure 1. 3D model of pixelated CdTe sensor.

The overall spectrum generated by the photon beam was obtained from Spektr 3.0. The spectrum was generated using the TASMIP model with 120 kV tube potential [1]. To simplify the simulation, we assume that photon tracks are perpendicular to the sensor surface. Each photon interacts randomly within the central pixel, and its interaction depth is calculated based on the exponential distribution using the corresponding mean free path from XCOM database [2]. We assumed that photons interact only by photoelectric absorption because the cross-section of the photoelectric

effect in X-ray spectrum is much higher than the cross-section of Compton scattering. Also, we assumed that the initial charge cloud generated by the incident photons is point-like, and then it spreads due to diffusion in the sensor. Therefore, we expect Gaussian charge cloud shape with sigma:

$$\sigma = \sqrt{2Dt_{drift}} \tag{1}$$

where D is the diffusion coefficient of electrons in CdTe and t_{drift} is the time for which the electron cloud drift until it reaches collection electrodes. The t_{drift} depends on the interaction depth - the closer the interaction to the collection electrode, the shorter the drift time. The drift time for all interaction depths was calculated based on 3D TCAD simulation. After each interaction, the charge collected by the central pixel is found and converted to photon energy. Finally, the internal counter corresponding to this energy is incremented. The simulation steps are repeated till the spectral response of the sensor is obtained.

3. RESULTS AND DISCUSSION

To demonstrate the effects of charge diffusion and fluorescent photons separately, we prepared three types of simulation: The first situation, Figure 2 – (a), only charge diffusion is taken to account. The generated electron cloud spread across the neighboring pixels causing a spectrum shift toward the lower energies. The second situation, Figure 2 – (b), corresponds to the situation where one fluorescent photon is generated. The spectrum is more shifted towards the lower energies, and the fluorescent photons appear as peaks in other pixels. Figure 2 – (c) shows the third situation when the possibility of the generation of two fluorescent photons is added to the simulation. This leads to an even more shift towards lower energies.

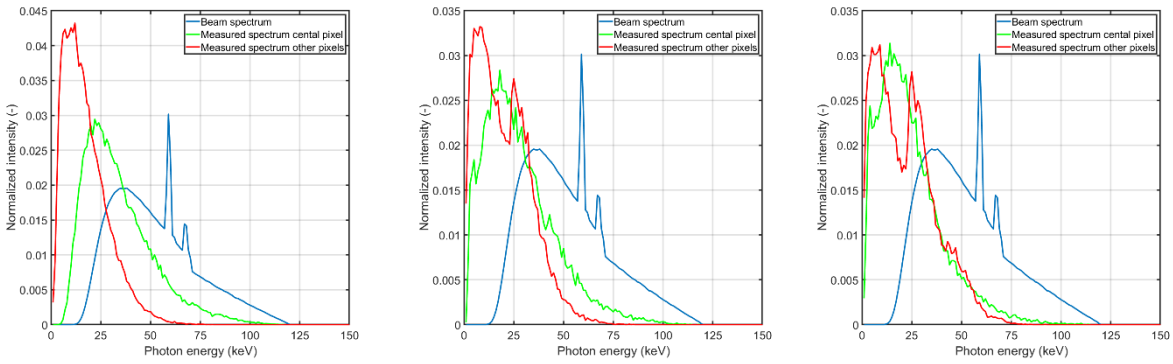

Figure 2. Effects of charge diffusion and fluorescent photons on the spectrum (a) – only charge diffusion (b) – charge diffusion and fluorescent photon (c) – charge diffusion and two fluorescent photons.

ACKNOWLEDGMENT

This work was supported by the Centre of Advanced Applied Sciences CZ.02.1.01/0.0/0.0/16-019/0000778, co-financed by the European Union and Czech Grant Agency of the Czech Technical University in Prague, grant SGS20/175/OHK3/3T/13.

REFERENCES

[1] J. Punnoose, J. Xu, A. Sisniega, W. Zbijewski, and J. H. Siewerdsen, "Spektr 3.0-A computational tool for x-ray spectrum modeling and analysis," *Med. Phys.*, vol. 43, no. 8Part1, pp. 4711–4717, Jul. 2016.

[2] M. J. Berger *et al.*, "XCOM: photon cross sections database," *NIST Standard Reference Database*,1998. Available: http://physics.nist.gov/PhysRefData/Xcom/Text/XCOM.html.

ANALYSIS OF THE OPERATOR'S PILOT MODEL WHEN CONTROLLING THE UAV IN THE LONGITUDINAL PLANE

R. Bréda[1], Š. Karaffa[1], M. Hlinková[1]

[1]Technical University of Košice, Faculty of Aeronautics / Department of Avionics, Košice, Slovensko
robert.breda@tuke.sk, simon.karaffa@tuke.sk, miriam.hlinkova@tuke.sk

1. INTRODUCTION

The abstract presents an analysis of the characteristics of the pilot's operator in the control of a small unmanned aircraft in the longitudinal plane at selected speeds of 90 km/h. The observed parameter is the response of the pilot in the control circuit of a small unmanned aircraft of longitudinal inclination to the required value. Types of models are selected based on the required human characteristics for machine control. We can use the type of model with regard to the speed of human reaction, control accuracy, etc. Examples are the types of mathematical models of operator pilots in the form of an open pilot model with a parallel block, a closed pilot model with a variable structure, or an open pilot model with a variable structure and a nonlinear term, which is used to solve complex control tasks.

2. METHODS AND RESULTS

Small unmanned aircraft pilot operator must perceive and process various information and be able to react to any situation during flight [1]. In UAV control, the operator's pilot is not affected by the same variables as the pilot in the aircraft control circuit, but some sensory organs need to be used to manage UAV control and stable flight. The sensory organ that the pilot operator mainly uses to control the UAV is visual. It is necessary for the operator to have good motor characteristics. These features need to be included in the UAV pilot's mathematical model, which is described in [1] [2].

$$F_{(s)} = \frac{Y_{(s)}}{X_{(s)}} = K\frac{(T_3 s + 1)}{(T_1 s + 1)(T_2 s + 1)} e^{-\tau s} \quad (1)$$

K – pilot gain factor, τ – pilot delay response to received signal, T_1- time value that represents learned stereotypes, T_2- nerve muscle time, which represents the delay of muscular and sensory organs working at the level of the spine, T_3- time value that defines the pilot's experiences.

The time value representing the learned stereotypes and the time value defining the pilot's experience will be the same [2]. Nerve muscle time will be lower because the UAV pilot's effort to drive is less, it is not necessary for the operator to use spinal-level muscle organs.

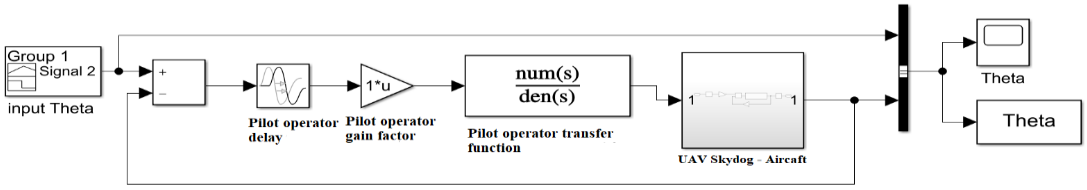

Figure 1. Pilot operator model with UAV Skydog

The main parts of the simulation model (Figure 1) are the transfer functions of the pilot and the transfer function of the UAV in which the actuator, the PID controller with feedback, is included [3]. The aircraft transfer function characterizes the dynamics of the aircraft, which responds to the input signal and to the pilot control. The action variable is the angle of deflection of the control surface

and the actuator is the servo that performs this movement. By obtaining the transfer functions of the actuator and the aircraft itself, it is possible to calculate the PID coefficients of the controller for a given system. The values of the PID controller coefficients depend on the coefficients of the transfer function of the system. The transfer function of the actuator is fixed unless we consider a system failure or change in its properties. As a result of the change in airspeed, the aerodynamic forces and moments acting on the airplane as well as the coefficients of the airplane transfer function change. We consider the state at a speed of 90 km/h to be the ideal state in which the controller works best.

$$F_{\dot{\vartheta}_{90}}^{\delta_v} = \frac{61{,}7s+28{,}43}{s^2+4{,}482s+1{,}41} \tag{2}$$

By changing the speed, the coefficients of the transfer function change [3]. Flight speed 90 km/h was chosen because it is the cruising speed of the UAV "Skydog" and so a substantial part of the experimental flights take place at approximately this speed [4].

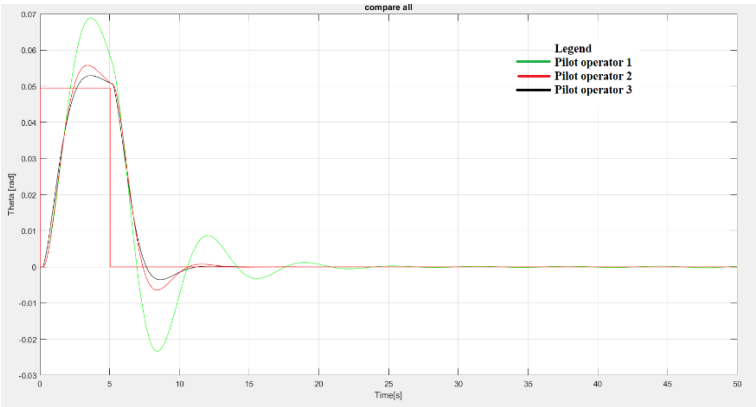

Figure 2. Modeled pilot reactions in longitudinal stability at 90 km / h

Figure 2 shows the individual Theta waveforms that visualize the reactions of individual pilots to the UAV Skydog at a speed of 90 km/h. The reactions of pilots 1, 2 and 3 are time constants that define the experience and skills of the pilot, where it is seen that pilot 2 has the best process.

3. CONCLUSION

The abstract analyzes the mathematical model of the pilot operator. Figure 2 compared the characteristics of the pilot operators. Figure 2 also shows the difference between the transfer functions of the pilot operators, which were set according to the assumed experience and knowledge transferred to the time variables. It is recommended to compare all the results of the simulation model with a human pilot operator on the simulator.

REFERENCES

[1] McRuer, D. T., Krendel, E. S.: Mathematical Models of Human Pilot Behavior, AGARD AG-188, 1974.

[2] Jalovecky, R., Janu, P., Boril, J.: Experimental Parameters Identification of the Human-Pilot Model Behaviour, Cybernetic Letters 1 (2016).

[3] Roskam, J.: Airplane Flight Dynamics and Automatic Flight Controls - Part I, Third Printing. Lawrence, Kansas: DAR corporation, 2001. ISBN 1-884885-17-9.

[4] Hess, R. A.: Modeling Pilot Control Behavior with Sudden Changes in Vehicle Dynamics, Journal of Aircraft 46 (2009), 1584–1592.

POLYMER PLANAR BRAGG GRATINGS BASED ON BULK CYCLIC OLEFIN COPOLYMERS: FABRICATION AND FUNCTIONALIZATION

Stefan Kefer[1], Bernhard Schmauss[2], Ralf Hellmann[1]

[1]Applied Laser and Photonics Group, Aschaffenburg University of Applied Sciences, Wuerzburger Strasse 45, 63743 Aschaffenburg, Germany
[2]Institute of Microwaves and Photonics, University of Erlangen-Nuremberg, Cauerstrasse 9, 91058 Erlangen, Germany
E-mail: stefan.kefer@th-ab.de

1. INTRODUCTION

The impact of polymer planar optical sensors and integrated photonics has increased significantly throughout recent years. Especially Bragg grating concepts have drawn the interest of scientists around the world. However, most standard polymers, such as polymethyl methacrylate (PMMA) or polycarbonate (PC) suffer from inadequate temperature resistance and / or an undesirable cross-sensitivity towards humidity. This drawback can be overcome by employing cyclic olefin copolymers (COC) as substrate material. Besides glass transition temperatures up to 250 °C, they also offer negligible water absorption, outstanding solvent resistance and blood compatibility [1]. Furthermore, injection-molded, and thus reasonably priced substrates can be employed for the fabrication of COC-based polymer planar Bragg gratings (COC-PPBG).

2. FABRICATION AND FUNCTIONALIZATION OF POLYMER PLANAR BRAGG GRATINGS

A sophisticated single-writing-step (SWS) procedure is employed to manufacture COC-PPBGs. The principal methodology is outlined in Figure 1 (a)

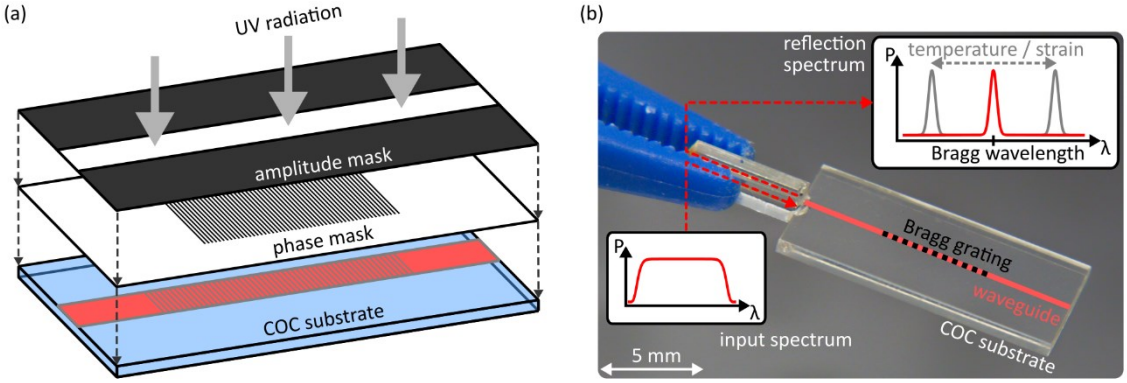

Figure 1. (a) Fabrication via single-writing-step method and (b) working principle of a COC-based polymer planar Bragg grating.

After forming a stack, consisting of a COC substrate, a phase mask and an amplitude mask, the sample is irradiated with UV radiation generated by a krypton fluoride laser. The employed process parameters are a pulse energy of 68 µJ and a pulse duration of 15 ns at a repetition rate of 200 Hz. For most applications, the overall fluence ranges from 100 to 200 J cm^{-2} in order to achieve a COC-PPBG with optimum signal properties. Afterwards, the COC specimen is thermally treated at a temperature of 130 °C for a duration of two hours. This leads to the formation of a waveguide comprising a periodic refractive index modulation, or Bragg grating, buried underneath the substrate surface [2]. A COC-PPBG generated by means of the SWS procedure as well as its working principle is depicted in Figure 1 (b). When Broadband light is coupled into the PPBG's photonic

structures, the Bragg grating serves as a narrow bandwidth reflector. Its wavelength of main reflection, also denoted as Bragg wavelength λ_B, strongly depends on the grating's effective refractive index n_{eff} and its periodicity Λ according to

$$\lambda_B = 2n_{eff}(T,\varepsilon)\Lambda(T,\varepsilon). \quad (1)$$

Since both, n_{eff} and Λ, are functions of temperature T and strain ε, a change of these physical properties leads to a proportional Bragg wavelength shift $\Delta\lambda_B$, which can be evaluated for sensing purposes [3].

Furthermore, by means of subsequent functionalization, COC-PPBGs can be adapted and optimized for a new range of applications. For example, a Pt-loaded WO_3-SiO_2 coating enables the hypersensitive detection of molecular hydrogen concentrations, down to 5 ppm (0.0005%) of H_2 in air [4]. The response curve of such a device is shown in Figure 2 (a).

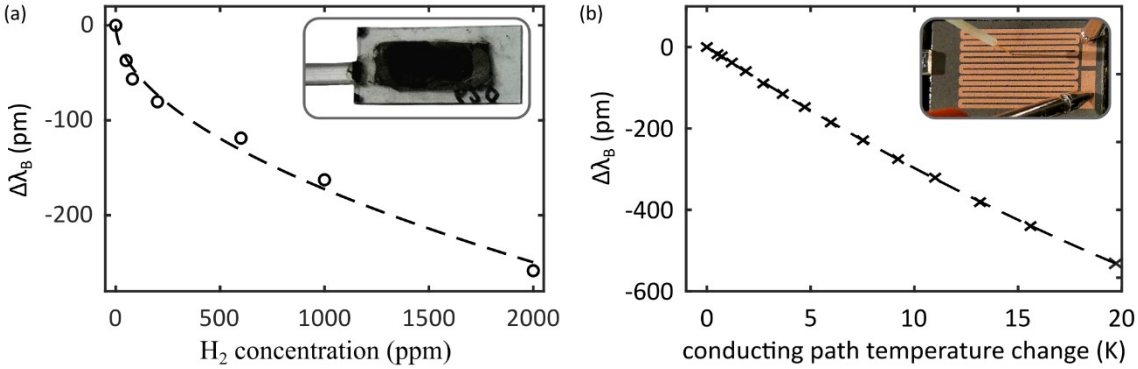

Figure 2. (a) Response of a COC-PPBG functionalized for H_2 sensing. (b) Wavelength tuning response of an electrified COC-PPBG. The respective functionalized PPBG is shown in each inset.

By means of femtosecond laser reductive sintering of a copper(II) oxide nanoparticle solution, it is also possible to equip the COC-PPBG's surface with a conducting path. As shown in Figure 2 (b), the device's Bragg wavelength is actively tuned by exploiting the conducting path's heat losses. Thus, it can be used as an electro-optic tunable filter device [5].

3. CONCLUSION

This contribution summarizes on PPBGs based on COCs. The employed fabrication method, denoted as single-writing-step procedure, is outlined. Furthermore, an overview on generating COC-PPBG-based hydrogen sensors as well as electro-optically tunable devices is given. Finally, an insight into each specimen's performance is also provided.

REFERENCES

[1] Khanarian, G.,: 2001, Optical properties of cyclic olefin copolymers, Optical Engineering 40, pp. 1024–1029.

[2] Rosenberger, M., Koller, G., Belle, S., Schmauss, B., and Hellmann, R.,: 2012, Planar Bragg grating in bulk polymethylmethacrylate, Optics Express 20, pp. 27288–27296.

[3] Kashyap, R., *Fiber Bragg Gratings*, 2nd ed. (Academic Press, 2010).

[4] Kefer, S., Dai, J., Yang, M., Schmauss, B., and Hellmann, R.,: 2020, Hypersensitive H_2 Sensor Based on Polymer Planar Bragg Gratings Coated with Pt-Loaded WO_3-SiO_2, Optics Letters 45, pp. 3601–3604.

[5] Kefer, S., Bischoff, K., Roth, G.-L., Haubner, J., Schmauss, B., and Hellmann, R.,: 2021, Tunable Bulk Polymer Planar Bragg Gratings Electrified via Femtosecond Laser Reductive Sintering of CuO Nanoparticles, Advanced Optical Materials, p. 202002203.

DIGITAL GUITAR PEDAL

Jakub Turinský, Jan Holub

Czech technical university in Prague,
Faculty of Electrical Engineering, Department of measurement
turinjak@fel.cvut.cz

1. INTRODUCTION

The article deals with design, testing and measurement a digital guitar pedal with an analog effect module that can be used as a fully functioning pedal or a versatile development unit. The author created a device with several functions and the possibility to modify the firmware. An uncommon feature that was required is control of the sound processor input volume via an external expression pedal. The core of the finished pedal was based around the FV-1 sound processor and will include a slot for an effect module that I designed with the KHDK company to combine analog and digital effects in one unit. The project did not include audio effect program design and was tested on open source programs available online [1].

Figure 1: Photo of finished prototype with overdrive effect module both with true bypass switching

2. METHODS AND RESULTS

The main circuit is based on the FV-1 typical application circuit [2] and open-source development kit from PedalPCB [3] company that includes PCB that I assembled and tested. The traditional way of a buffered bypass is to disconnect the signal path before and after the sound processor because they are usually disconnected by a mechanical switch (which makes pop sound) or by JFET (which lets amplified signal through). My buffered bypass works by switching a photorelay TLP222g for a noiseless result. The controlled relay used for the bypass switching has a muting photorelay TLP222g on the output, which mutes the output of the relay for a short time, making the switching noiseless. The controlled buffered bypass is noiseless on its own, so it doesn't need to be muted. I based the controlled bypass on an open-source project from Mark A. Stratman [4].

The effect unit is designed to fit into the Hammond 1590BB enclosure with mechanical support through electromechanical components. Apart from a custom USB programmer for 24LC32A EEPROM, I designed an Attiny programmer shield for Arduino UNO and a very simple shield for Leo oscilloscope for easier electronic debugging.

3. CONCLUSION

I designed, tested, and measured a digital guitar pedal with an analog effect module that can be used as a fully functioning pedal or a versatile development unit. It is reprogrammable by a custom external USB programmer, that enables almost complete SMD assembly. I designed four fully functioning bypass possibilities – True bypass, buffered bypass, controlled relay bypass with pop noise muting, and controlled buffered bypass by Attiny85 processor. Controlled relay bypass switching has integrated muting of pop noise on the output, so it is noiseless. Buffered bypass works in an unusual way where when bypassed, the signal on the sound processor output fades out naturally without any noise repeated by switching. The guitar pedal includes expression input for control of theFV-1 input volume. My design consists of all necessary custom-made PCB subboards for a fully functioning and serial manufacturable result. The whole project was designed to be as cost-effective as possible for future manufacturing.

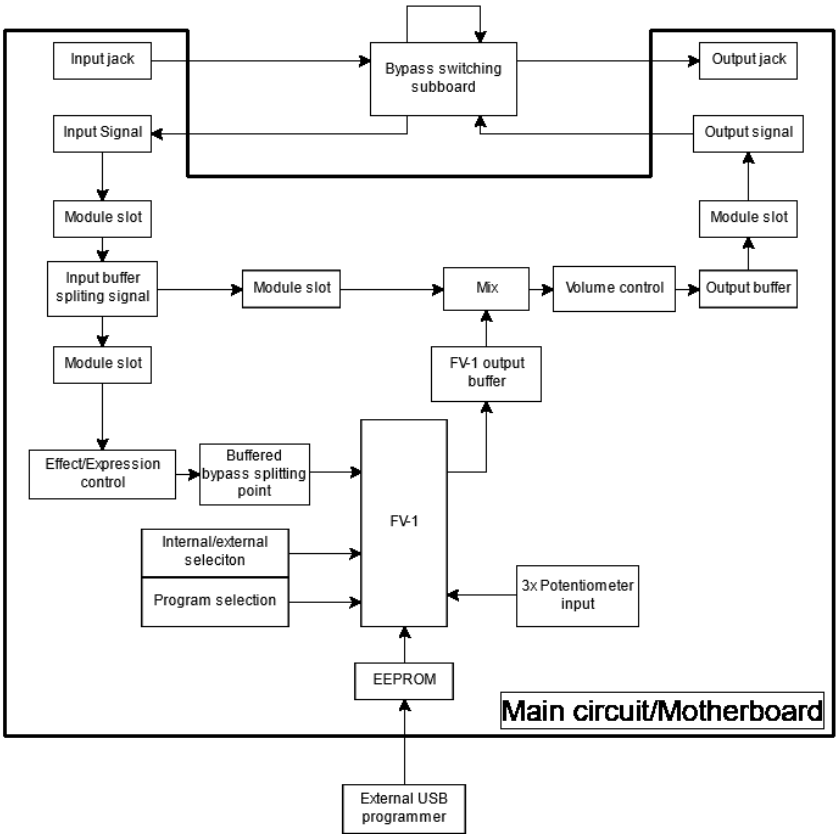

Figure 2: Guitar pedal block diagram

ACKNOWLEDGMENT

The authors would like to express appreciation for the support of the sponsor KHDK company for hardware support and sponsoring the development costs.

REFERENCES

[1] Mark A. Stratman: 2021, FV-1 Programs, available at: https://mstratman.github.io/FV-1-programs/

[2] Spin Semiconductor: 2021, FV-1 Reverb IC Featuring Spin Semiconductor Virtual Analog Technology, available at: http://www.spinsemi.com/Products/datasheets/spn1001/FV-1.pdf

[3] PedalPCB: 2021, FV-1 Development PCB, available at: https://www.pedalpcb.com/product/fv1dev/

[4] Mark A. Stratman: 2021, Soft touch relay bypass for DIY guitar pedals, available at: https://github.com/mstratman/relay-bypass

Proton magnetometer and precession signal processing

Bc. Ondřej Bureš, Ing. Vojtěch Petrucha, Ph.D.

CTU in Prague, Faculty of Electrical Engineering
bureson1@fel.cvut.cz, petruvoj@fel.cvut.cz

1. INTRODUCTION

Today, several methods can be used to measure the Earth's magnetic field. For example, vector magnetometers based on the principle of magnetoresistance are often used due to their lower price and power consumption. In case of measuring with higher accuracy, fluxgate magnetometers are more appropriate. The drawback of vector magnetometers is their dependence on temperature. For this reason, scalar magnetometers based on the principle of proton precession, referred as proton magnetometers, are in some cases more suitable. This type of scalar magnetometer depends only on the magnetic induction and the gyromagnetic constant. For this reason, they are ideal for example for calibration of mentioned vector magnetometers.

The aim of this project is to design and realize proton precession magnetometer intended for Earth's magnetic field measurements with the possibility of signal sampling for subsequent data analysis. Main motivation is to compare different frequency measurement methods, verify the principle of the proton precession magnetometer, and in the future to use the constructed device as a in-field calibration unit for a precise vector fluxgate magnetometer.

2. METHODS AND RESULTS

2.1 Magnetometer design and realization

The constructed device consists of three separate systems, namely sensor, switching circuit and signal processing circuit. This separation allows testing of more configuration types with different sensors and switching circuits. Connection of three mentioned systems can be seen in figure 1.

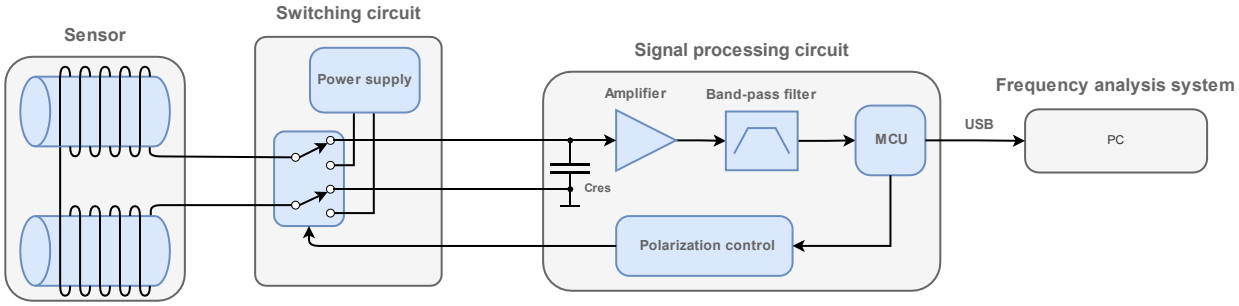

Figure 1. Block diagram of constructed magnetometer.

For our purposes two sensors were used. First one was constructed here at CTU in MAGLAB and the second one is a commercial PM-2 from Geofyzika Brno.

The most common switching circuit uses combination of relay and transistor. Since relays have a limited lifetime, they are not suitable for observatory application. Because of that, two different switching circuits were used and compared. The first switching circuit uses relay and is based on already constructed magnetometer that can be found on MagLab websites *[1]*. The second implementation of switching circuit uses a configuration of MOSFET transistors and does not need a presence of relay *[2]*. However, its disadvantage is that it provides lower amplitude of precession signal.

2.2 Precession signal analysis

In order to determine the frequency of precession signal, three different methods were used. One of them uses a combination of a comparator and timer in input capture mode with a frequency $216\ MHz$. In case of precession signal frequency $2\ kHz$ the resolution of used timer is less than $19\ mHz$, as is shown in Eq. [1].

$$\frac{216\ MHz}{108\,000} - \frac{216\ MHz}{108\,001} \approx 18.5\ mHz \tag{1}$$

Other two methods were fast Fourier transform (FFT) and construction of Analytical signal using Hilbert transformation. In both cases it is inevitable to have a sampled signal to obtain the resulting frequency. For this reason, 16-bit ADC with sample rate of 44.1 kHz was used. Since the precession signal takes no longer than one second, the frequency resolution of FFT would be in best case 0.5 Hz, as is shown in Eq. [2]. To increase the frequency resolution of FFT it is possible to use zero-padding technique [3]. This interpolation helps to identify the peak in frequency-domain more precisely.

$$\Delta f = \frac{F_s}{N} = \frac{44100}{2 \cdot 44100} = 0.5\ [Hz] \tag{2}$$

For frequency analysis purpose, we can also use Hilbert transform to construct the analytic signal. Using this technique, it is possible to determine instantaneous and afterwards an average frequency [4].

2.3 Achieved results

In order to perform real testing of constructed magnetometer and to compare effectivity of three different frequency analysis methods, we measured the Earth's magnetic field in Pruhonice village. The achieved maximal and minimal standard deviations using four different configurations are shown in Table 1. The best results were obtained using switching circuit with relay and commercial sensor.

Table 1. Achieved minimal and maximal standard deviations using different system configurations

	FFT (BIN WIDTH 10 MHz)	FFT (BIN WIDTH 100 MHz)	COMPARATOR	HILBERT TRANSFORM
σ_{min}	0.35 nT	0.72 nT	0.57 nT	0.69 nT
σ_{max}	1.54 nT	1.74 nT	78.1 nT	111.35 nT

2 CONCLUSION

The aim of this project was to design and realize proton precession magnetometer intended for Earth's magnetic field measurements and compare different methods of frequency analysis. For measuring purposes, four different configurations were used, and the minimal standard deviation 0.35 nT was achieved using FFT with zero-padding. The future plans are to improve the relay-less switching circuit to deploy the constructed device in Kasperske hory for daily measurements.

REFERENCES

[1] Ing. Vojtěch Petrucha, "MagLab," [Online]. Available: https://maglab.fel.cvut.cz/workshop /proton-magnetometer/.

[2] J. A. Koehler, "Proton Precession Magnetometers, Rev. 3," pp. 40 - 43, 2012.

[3] D. Related, "ZERO PADDING IN THE TIME DOMAIN," [Online]. Available: https://www.dsprelated.com/freebooks/sasp/Zero_Padding_Time_Domain.html.

[4] B. Boashash, "Estimating and interpreting the instantaneous frequency of a signal. I. Fundamentals," *Proceedings of the IEEE*, vol. 80, no. 4, pp. 520 - 538, 1992 .

RADIATION TESTING OF A STUDENT-DESIGNED CUBESAT OBC

Geib, F[1], Petrucha, V[1]

[1]Facultry of electrical engineering, CTU in Prague
geibfili@fel.cvut.cz

1.INTRODUCTION

Occasionally traveling through weaker parts of the Earth's magnetic field and not shielded by the Earth's atmosphere, the CubeSats have to operate in an environment full of radiation. A direct hit of a high-energy particle might have severe consequences for their onboard electronics.

In a previous project, we have successfully designed an onboard computer (OBC) dedicated to the PC/104 format Cubesats. Its design is based on commercial off-the-shelf (COTS) components without any radiation hardening. Therefore we were interested in how well the OBC performs in a radiation-rich environment and what total dose it can overcome. On top of that, we were also interested in similar characteristics of some COTS acceleration and magnetic field sensors.

2.METHODS AND RESULTS

2.1. Tested OBC and sensors

The experiment was performed on an OBC known as a Board Sierra [1]. This ARM-based OBC accommodates a single STM32L496 microcontroller with not rad-hardened architecture.

Together with the OBC, we tested another four electronic sensors: i) one piece of always-on 3D accelerometer and 3D gyroscope LSM6DS3, ii) two pieces of high-performance 3-axis magnetic sensors MMC5983MA, and iii) one piece of integrated 6-axis motion processor with gyroscope and accelerometer MPU6050. Each of these sensors had a separate switchable power input (controlled by the OBC) and communicated with the OBC through an I^2C bus.

2.2. Software loop

The testing software was developed in the C language using the STM32CubeIDE. The measurements and testing were conducted in one continuous loop, executed with frequency 2[Hz]. Logs of measured data or potential errors were sent via two independent UART channels. If a sensor reading encounters an error, the software forced the sensor hardware power reset in the following loop. A prevention power reset of all sensors was conducted every ten minutes.

2.3. Experiment setup

The experiment was conducted in one of the facilities of the nuclear research institute ÚJV Řež. The OBC, together with the sensors, were mounted on a testbed (see figure 1) and placed inside a cobalt-60 gamma radiation source. The testbed was left exposed to radiation for three days. After the experiment, the carried nominal radiation dose was determined as 4.8[krad/hour].

During the entire experiment, two independent UART devices were used for logging the OBC's outputs. Three current monitoring resistors (so-called shunt resistors) were attached directly to the OBC and the sensors' power inputs, continuously measuring the consumed power. This was achieved with a data acquisition module PXIe-4303 DAQ installed in a PXIe-1082 frame. Also, a watchdog circuitry was implemented to manage the power delivery. In an active state, the OBC was permanently toggling a watchdog signal to indicate its well-being. If this toggling disappeared, the watchdog circuitry disconnected the power busses in order to force theOBC's power reset.

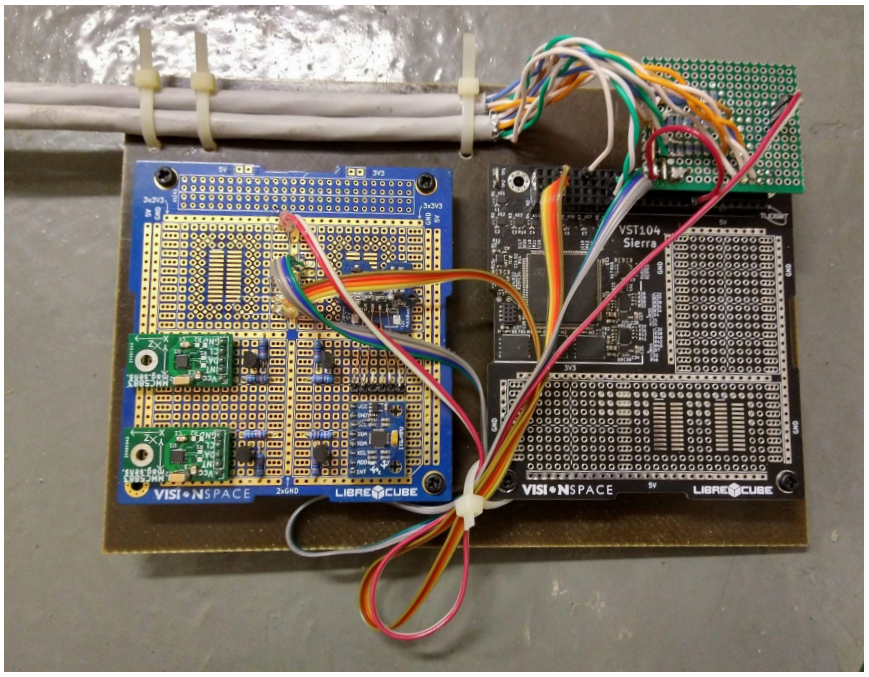

Figure 1. Photograph of the tested electronics mounted on a testbench. Visible is a blue board with individual sensors (left) and a black-colored OBC (right). The green PCB accommodates shunt resistors and cable management.

2.4. Experiment results

Approximately at 5.20[hour] after the beginning of the experiment, the OBC started to malfunction. Until this point, it performed normally without a single error. The total radiation dose at this point sums up to 24.96[krad]. Then, the OBC entered a continuous restart loop of about 100[Hz], managing to send only one UART log per restart. It booted successfully again at 5.27[hod], after 4.2[min] from the first malfunction. After some initial errors and a couple of reboots, it operated well without a single problem until its last log at 5.30[hour]. After that, the UART received dozen of broken characters, and the OBC stopped responding at 25.44[krad].

The first and only sensor that stopped performing normally was the LSM6DS3. After 4.02[hour] from the experiment start, the sensor stopped answering measurement requests. This corresponds roughly to a 19.29[krad] total radiation dose. However, after multiple power resets and few faulty readings, the sensor started to behave well again at 5.30[hour] of the experiment.

3.CONCLUSION

We have tested and examined the radiation tolerance of the Board Sierra OBC and mentioned COTS sensors. The obtained results show that these devices can perform well in a radiation-rich environment. The OBC encountered its first problems at circa 25[krad], the LSM6DS3 at 12.3[krad], and the other sensors performed without any malfunction.

It is although important to note that not all data have been reviewed so far. We will finish their processing and analysis by the conference and then submit an abstract revision.

ACKNOWLEDGMENT

The authors acknowledge the support of the ÚJV Řež, a.s. to permit the use of their research facility, namely Martin Cabalka Ph.D. and Vít Plaček Ph.D.

REFERENCES

[1] Visionspacetec. (n.d.). visionspacetec/VST104-Sierra. GitHub. https://github.com/visionspacetec/VST104-Sierra.

AN ENERGY-EFFICIENT SELF-OSCILLATING FLUXGATE SENSOR FOR DC CURRENT MEASUREMENT

Václav Grim[1], Pavel Ripka[1]

[1]Department of Measurement, Czech Technical University
vaclav.grim@fel.cvut.cz (corresponding author)

1. ABSTRACT

A novel circuit suitable for high precision, contactless current measurement based on nonlinear magnetic properties of a ferromagnetic core material is presented. It provides a robust, cycle-by-cycle current limiting method to periodically saturate the core in alternating directions. Its performance was evaluated and compared with other methods, in particular the traditional second harmonic detection.

2. INTRODUCTION

Contactless current measurement is possible with several different methods, all of them are based on measuring the magnetic field around the conductor. For large currents (hundreds of Amperes and more), magnetooptical transducers are the most modern, although expensive, approach. For smaller currents or for lower cost applications that need to sense DC current as well, closed-loop Hall sensors or fluxgate sensors are used. Fluxgate-based current transducer works the same way as a fluxgate magnetometer, but instead of measuring the field magnitude along a particular vector of sensitivity it measures along a closed loop, where the flux density is given by the Ampere's law. For acceptable linearity and wide measurement range, such sensors usually work in compensated mode, where the fluxgate is used as a null detector, adjusting a current through the compensation winding to yield a zero flux density in the core.

3. MAGNETIC DESIGN

The transducer consists of one toroidal core made of a nanocrystalline alloy (Vacuumschmelze Vitroperm 500F). Its diameter was selected to allow a sufficiently thick conductor to pass through the center. The excitation winding has 60 turns and it serves also as a pickup winding. The turns count was calculated as to achieve 10 times the saturation field intensity at approximately 500 mA excitation current peak. The feedback is obtained by observing the integral of the excitation current. The positive and negative peak value of the current is fixed, but its mean value depends on the primary current.

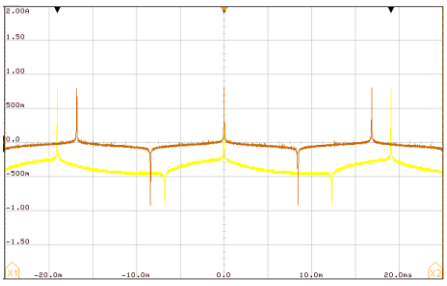

Figure 1. Excitation current with zero primary current (red trace) and with 20 A primary current, feedback loop disconnected (yellow trace)

The mean value of the excitation current is used to control the compensation current. The compensation current is fed into a separate winding with 60 turns. Therefore, the ratio of measured

and compensation current is always precisely 1:60, as long as the feedback loop keeps the integrator at zero voltage.

4. ELECTRIC DESIGN

The excitation winding is driven with a square wave voltage provided by an H-bridge with a single current sense resistor at the bottom. The control signals are generated by a simple T flip-flop which changes state each time the voltage across the sense resistor crosses a predetermined threshold.

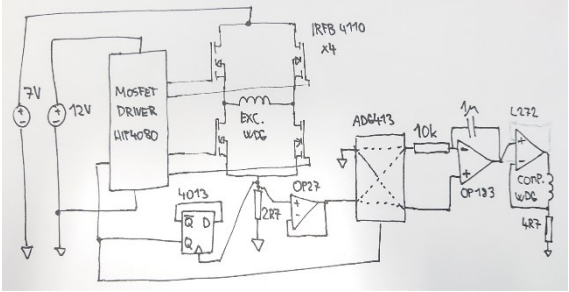

Figure 2. Excitation current with zero primary current (red trace) and with 20 A primary current, feedback loop disconnected (yellow trace)

Because switching the H-bridge polarity reverses the current through the sense resistor relative to the winding, another commutation of the sense voltage with a CMOS analog switch is performed before integrating. The integrated voltage controls a high power operational amplifier connected as a constant current source. This amplifier needs to maintain the desired current at the presence of the excitation voltage multiplied by turns ratio, which limits the usable number of turns in the compensation winding.

5. VALIDATION AND CHARACTERIZATION

A test stand with 2 meter long straight aluminum bar, powered with 1.2 kA power supply was used to provide test current. Values measured with a LEM IT-60 transducer were used as a reference. Linearity was tested between -10 and +10 A. The range is limited by the maximum possible compensation current.

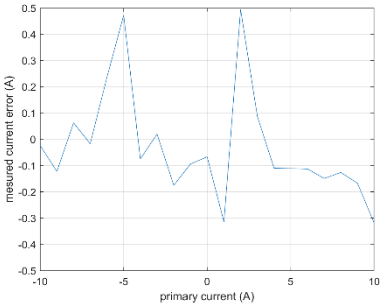

Figure 3. Measured transfer characteristic

6. CONCLUSION

Although the square wave excitation minimizes losses in the excitation circuit, more attention is required to address losses in the compensation circuit, where a linear amplifier with appropriate supply voltage causes a lot of unnecessary power consumption and heating.

ACKNOWLEDGMENT

This study was supported by the Grant Agency of the Czech Republic within the Nanofluxgate project (GACR GA20-27150S).

SIMULATION MODEL FOR A LOW COST HTS SQUID SYSTEM

Hall, T[1], Saunderson EF [1,2] , Fourie, CJ[1]

[1] Stellenbosch University, Stellenbosch, South Africa
[2] SANSA Space Science, Hermanus, South Africa

19775539@sun.ac.za

1. INTRODUCTION

Commercial high temperature superconductor (HTS) superconducting quantum interference device (SQUID) systems, which are used as extremely sensitive magnetometers, are prohibitively expensive if multiple SQUID measurement stations are planned. The HTS SQUID sensors are expensive due to thin-film fabrication requirements, and the control electronics are rendered expensive due to very low production volumes. HTS SQUID sensors are not off-the-shelf items, could have a manufacturing lead time of a year, and are extremely expensive due to the manufacturing process. In addition to sourcing a low-cost HTS SQUID device, it is important to design a custom FLL and control electronics.

2. METHODS AND RESULTS

2.1 SQUID magnetometer

A first step in this process is the simulation of a SQUID magnetometer to test the flux-locked-loop (FLL) and electronics design. To use the SQUID as a magnetometer for low frequency applications, a control system known as a flux-locked loop is required to linearize the SQUID transfer function while keeping added noise to a minimum. In a flux-locked loop, the SQUID voltage is amplified, lock-in detected, integrated, and fed back to the SQUID as a current through a feedback coil. The combination of flux modulation and bias current reversal in this control system ensures that the SQUID is biased at the points of lowest noise and that the 1/f noise due to critical current fluctuations is suppressed.

2.2 SPICE simulation of the full (FLL) SQUID system

The proposed design includes a low noise amplifier consisting of a bipolar input stage with a gain larger than one hundred and secondary amplification stages using low noise high precision operational amplifiers. The high gain of the input stage ensures that the noise produced in the subsequent amplification stages is essentially negligible. Lock in detection is achieved using synchronous switches with the product of the modulation and bias frequencies used as a reference signal. Both the integrator and secondary amplification stages are designed for flexibility to cater for different SQUID output ranges and allow for adjustments in the system's sensitivity.

The FLL system (SQUID bias, amplification and demodulation) has been simulated in LTspice with a dependent voltage source used to simulate a SQUID response to flux input – Fig. 1. The initial results have been very promising, with the V-Phi characteristics shown by the open-loop output of the flux-locked loop closely resembling the real V-Phi characteristics measured from an actual SQUID for a triangular flux input -- see Fig. 2. In addition, the simulated closed-loop output closely resembled the applied input flux waveform and the equivalent input noise of the FLL is quite low (in the region of 1 nV/√Hz). The end goal is to

produce dedicated low frequency SQUID readout electronics that are easy to control and implement. At this time only the design of the control electronics is considered, a commercial data acquisition unit will be used for data acquisition.

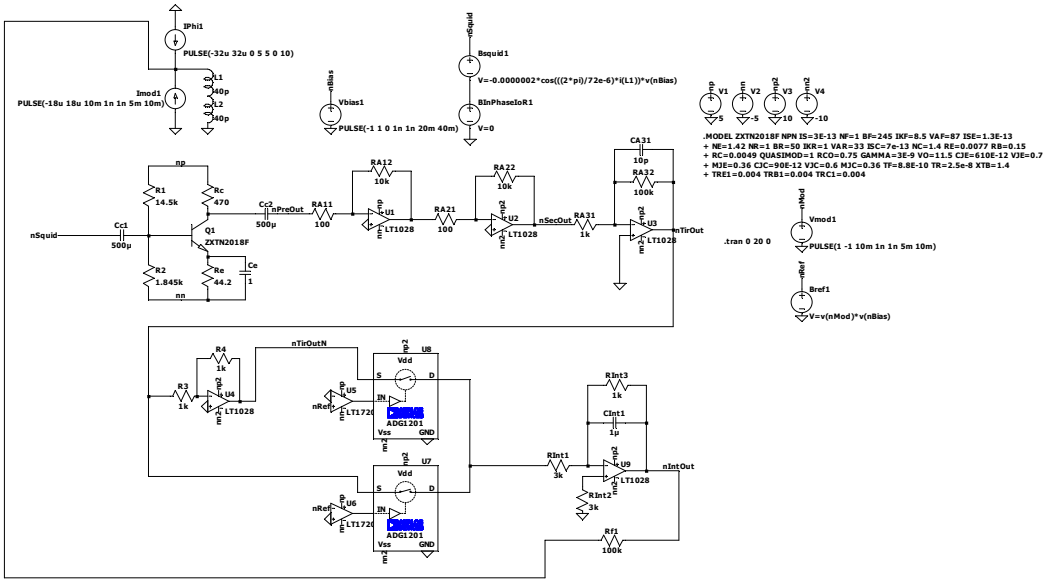

Figure 1. LTspice schematic of the flux-locked loop design

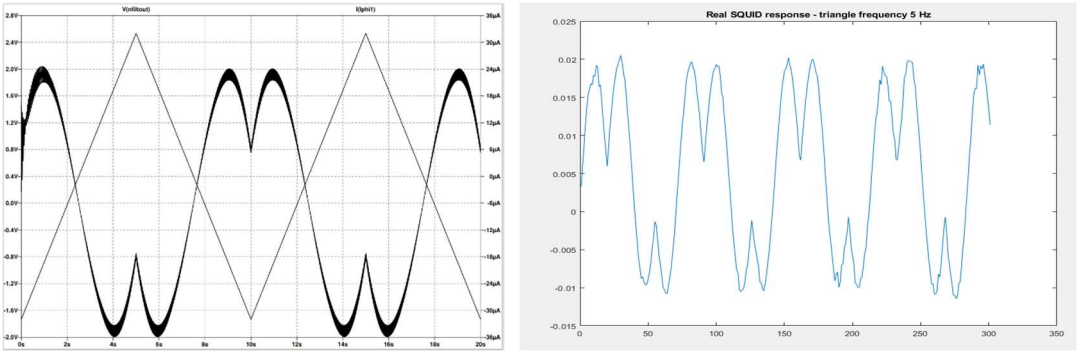

Figure 2. Simulated open-loop response at 100 mHz (left) and the real open-loop response of a M2700 SQUID measured unshielded at SANSA Hermanus (right)

3. CONCLUSION

The initial simulation results are promising with both the open and closed-loop waveforms resembling the expected output of a real SQUID. Transient simulations including noise produced in the FLL could provide better insight into the suitability of the design.

ACKNOWLEDGMENT

The authors would like to express appreciation for the support of the IEEE Magnetics Society who funded equipment through the Educational Seed Funding 2021.

REFERENCES

[1] Daalmans, G.M., 1995, "HTS DC SQUIDs for practical applications", Applied superconductivity, vol. 3.7, no 10, pp. 399-423.

[2] Clarke, J., Braginski, A.I., 2004, *The SQUID Handbook Vol. 1 Fundamentals and Technology of SQUIDs and SQUID Systems*, Germany: Wiley-VCH .

[3] Srinivas Kumar, B., et al, 1998, "Design and development of a flux-locked loop for low magnetic field measurements using dc squids", *IETE Tech. Rev.*, vol. 26, no. 3, pp. 209-216.

PARALLEL FLUXGATE SENSOR WITH AMORPHOUS WIRE CORE: SENSITIVITY STUDY

Hrakova, D[1], Ripka, P[1]

[1]Faculty of Electrical Engineering, Czech Technical University in Prague
hrakodia@fel.cvut.cz

1. INTRODUCTION

Traditional fluxgate sensors with wire core are using permalloy core material and three configurations: singe-core, Förster and Vacquier. We recently suggested several novel multiwire design configurations with the aim to increase the sensitivity and decrease the noise [1]. In this paper we present the results measured on amorphous wire cores.

2. METHODS AND RESULTS

The core wires were 0.12mm diameter amorphous with chemical composition $(Co_{94}Fe_{06})_{75}Si_{15}B_{10}$ manufactured by Institute of Technical Physics, Iasi, Romania and 0.2 mm diameter Permalloy Py wires with chemical composition Ni78Fe15Cu4Mo3 manufactured by Elidis, Czechia. The sensors were excited by HP 33120A generator and the output voltage was measured by the SR865 DSP 2 Mhz lock-in amplifier. The sensitivity was evaluated for 50 μT field step using the Helmholtz coils. The sensor noise spectrum density was evaluated by Agilent 35670A spectrum analyzer. The construction of the sensors and connection diagram are shown in Fig. 1.

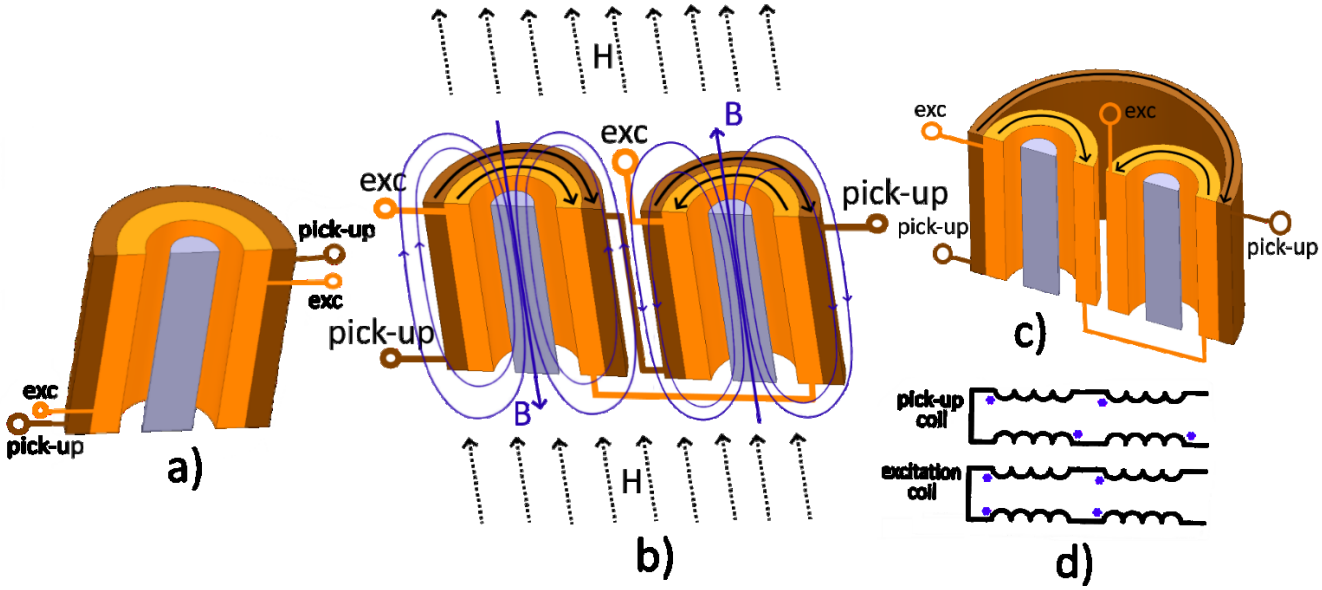

Figure 1. Fluxgate sensors with wire core a) Single-core b) Förster 1+1 c) Vacquier 1+1 d) connection of Förster 2+2

Single core sensor consists of 1 pick-up coil, 1 excitation coil, and a core which may consist of single or multiple wires. Sensitivity of such sensor as a function of number of wires for several excitation frequencies is shown in Fig. 2. For each case the excitation amplitude was adjusted to find the maximum sensitivity. Fig. 3 shows typical example of sensitivity dependence on the excitation voltage. Forster 1+1 and Vacquier 1+1 are traditional sensors, while all other sensors are using new multiwire design. The difference of between Single 2n and Förster/Vacquier n+n is that the latter has individual excitation coil for each wire.

Table 1 shows the coil parameters, Table 2 is an overview of the experimental results. The observed trends in sensitivity are in an agreement with simulation results.

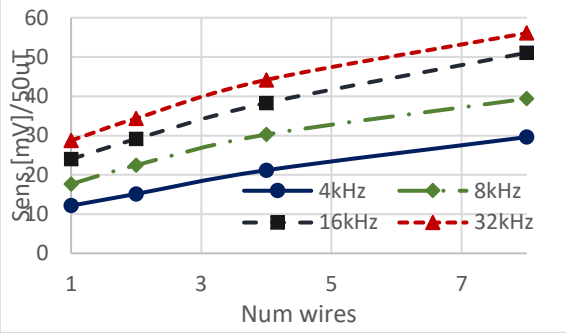

Figure 2. Single-core sensor: Sensitivity voltage vs. number of wires

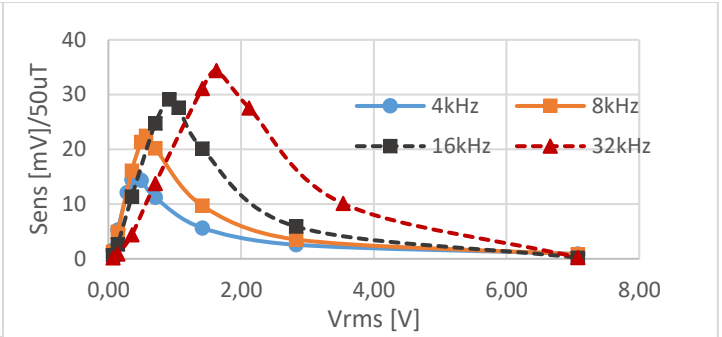

Figure 3. Single-core sensor with 2 wires: sensitivity vs. excitation

Table 1. Parameters of coils.

	Exc coils with diam = 0.5	Exc coils with diam = 0.35
N_exc	400	625
N_pick	200	300
D_exc	0.5 mm	0.35
D_pick	1.3 mm	0.8
D_winding_wire	0.2 mm	0.09
L	3.5 cm	3.5 cm
D core	0.12 mm	0.12 mm

Table 2. Results of measurements.

		4kHz		8kHz		16kHz	
		Max sens [mV]/ 50uT	Min noise [pT/√Hz]	Max sens [mV]/ 50uT	Min noise [pT/√Hz]	Max sens [mV]/ 50uT	Min noise [pT/√Hz]
	Permalloy Single 1	9.86	1470	15.04	1043	20.7	954
	Permalloy Forster 1+1	27.44	815	45.9	594	68.72	250
Amorphous	Single 1, d=0.5	12.15	109	17.65	110	24	93
	Single 2, d=0.5	15.138	125	22.45	161	29.14	187
	Single 4, d=0.5	21.17	125	30.26	138	38.3	281
	Single 8, d=0.5	29.6	195	39.38	243	51.09	497
	Single 1, d=0.35	20.8	97	30.22	125	38.86	174
	Forster 1+1, d=0.5	24.35	91	43.96	79	70.3	45
	Forster 2+2, d=0.5	46.38	80	87.7	45	127.17	44
	Vacquier 1+1, d=0.5	33.67	124	60.62	152	96.16	124
	Vacquier 2+2, d=0.5	63.62	58	112.9	73	180.5	49
	Vacquier 1+1, d=0.35	54.62	170	99.14	165	154.42	145
	Vacquier 2+2, d=0.35	120.3	70	207.7	74	309.3	52
	Vacquier 4+4, d=0.35	185.9	30	329.1	25	483.9	30

3. DISCUSSION AND CONCLUSIONS

Amorphous wires have 5-times lower noise compared to traditional permalloy wires. By using multiwire configuration the sensitivity can be increased by the factor of 10 and the noise can be reduced to 30 pT.

ACKNOWLEDGMENT

This study was supported by the Grant Agency of the Czech Republic within the Nanofluxgate project (GACR GA20-27150S).

REFERENCES

[1] P. Ripka, D. Hrakova, V. Grim, M. Mirzaei: Multiwire Parallel Fluxgate Sensors, Intermag 2021

COBALT NANOPARTICLES ANCHORED NITROGEN DOPED CARBON NANOTUBES FOR HIGHLY SENSITIVE SENSING OF HYDROGEN PEROXIDE

Yue Hu, A[1], Dongsheng Geng, B[1,2]

[1]Beijing Advanced Innovation Center for Materials Genome Engineering, Beijing Key Laboratory for Magneto-Photoelectrical Composite and Interface Science, School of Mathematics and Physics, University of Science and Technology Beijing, Beijing 100083, China
[2]School of Materials Science and Engineering, University of Science and Technology Beijing, Beijing 100083, China
dgeng@ustb.edu.cn

1. Abstract

Stable and highly sensitive determination of H_2O_2 is needed in many areas, from disease prevention to environmental protection. The construction of inexpensive and highly active transition-metal based nitrogen-doped carbon (TM-N/C) electrocatalysts for enzyme-free electrochemical detection of H_2O_2 is a promising approach. [1-2] Deriving TM-N/C electrocatalysts with abundant active sites and uniform micromesoporous from the rationally designed metal organic framework (MOF) as a self-sacrificing template has been verified as one of the most effective ways. [3-4] With this in mind, we report a general strategy based on the pyrolysis of the complex of nanosized bimetallic Zn/Co ZIF crystals and g-C_3N_4 for the spontaneous growth of nitrogen doped carbon nanotubes anchoring cobalt nanoparticles and atomic Co-Nx moieties (Co-N/CNTs). The existence of Zn^{2+} ions are served as "fences" to expand the adjacent distances of Co atoms, and evaporated away at high temperature of 920 ℃ to provide more opportunities to generate porous. Attributing to the synergetic contributions of the stable carbonaceous tubulose structure, high porosity and exposed abundant Co–N–C active sites, the further designed sensor exhibits excellent sensing performance towards H_2O_2 reduction with a wide linear current response range (concentration: 5×10^{-8} to 3.5×10^{-1} M), a low detection limit (3.11×10^{-8} M), a high sensitivity (1874.21 μA mM^{-1} cm^{-2}). Hence, the obtained Co-N/CNTs are provided with a practical application potential for detecting the concentration of H_2O_2 at a trace-level.

2. Figures

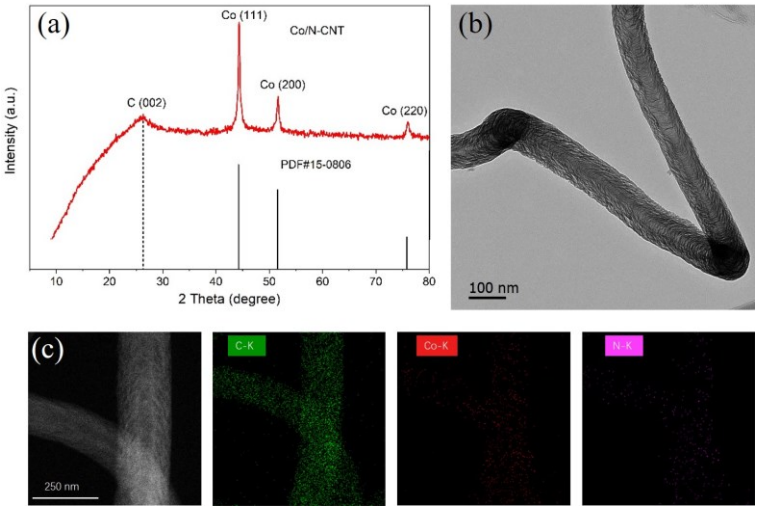

Figure 1. XRD pattern (a), TEM image (b), and EDX elemental mapping images of of Co-N/CNTs.

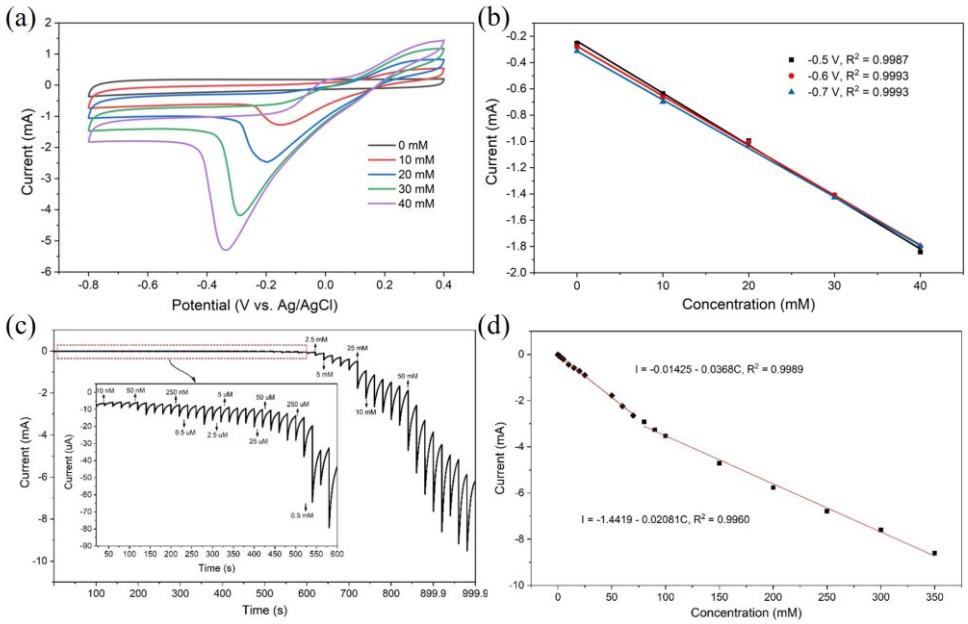

Figure 2. (a) CV curves of Co-N/CNTs based sensor with 0 × 10^{-3}, 10 × 10^{-3}, 20 × 10^{-3}, 30 × 10^{-3}, and 40 × 10^{-3} M H_2O_2, (b) Reductive current responses to different concentrations (0, 10, 20, 30, and 40 mM) of Co-N/CNTs at different voltages (-0.5 V, -0.6 V, and -0.7 V vs. Ag/AgCl), (c) i–t curves of Co-N/CNTs based sensor with H_2O_2 added successively, (d) the calibration plots of steady-state current versus different H_2O_2 concentrations of Co-N/CNTs based sensor.

REFERENCES

[1] Hassan, M., Jiang, Y., Bo, X.; Zhou, M.,: 2018, Sensitive nonenzymatic detection of hydrogen peroxide at nitrogen-doped graphene supported-CoFe nanoparticles, Talanta, pp. 339-348.

[2] Riaz, M. A., Yuan, Z., Mahmood, A., Liu, F., Sui, X., Chen, J., Huang, Q., Liao, X., Wei, L., Chen, Y.,: 2020, Hierarchically porous carbon nanofibers embedded with cobalt nanoparticles for efficient H_2O_2 detection on multiple sensor platforms, Sensors and Actuators B: Chemical, pp. 128243.

[3] Wu, Z., Sun, L.-P., Zhou, Z., Li, Q., Huo, L.-H., Zhao, H.,: 2018, Efficient nonenzymatic H_2O_2 biosensor based on ZIF-67 MOF derived Co nanoparticles embedded N-doped mesoporous carbon composites, Sensors and Actuators B: Chemical, pp. 142-149.

[4] Li, Z., Liu, R., Tang, C., Wang, Z., Chen, X., Jiang, Y., Wang, C., Yuan, Y., Wang, W., Wang, D., Chen, S., Zhang, X., Zhang, Q., Jiang, J.,: 2020, Cobalt Nanoparticles and Atomic Sites in Nitrogen-Doped Carbon Frameworks for Highly Sensitive Sensing of Hydrogen Peroxide, Small, pp. 1902860.

POSSIBILITIES OF USING MAGNETICALLY DETECTABLE FILAMENT FOR THE MAGNETORQUERS CORES PRODUCTION

Kašper, P[1], Fiľko, M[2], Šmelko, M, Čekanová, A, Szőke, Z

[1]Technical University of Košice, Faculty of Aeronautics, Košice, Slovakia
patrik.kasper@tuke.sk; martin.filko@tuke.sk; miroslav.smelko@tuke.sk; anna.cekanova@tuke.sk; zoltan.szoke@tuke.sk

1. INTRODUCTION

There are studies referring the impact of the magnetorquers core shape on its demagnetization effect which tend to be quantified in form of dimensionless coefficient called the demagnetization factor. According to these studies the most precise value of the demagnetization factor can be determined only in case of ellipsoidal shaped bodies. However, only prismatic, or cylindrically shaped ferromagnetic cores are used for the magnetorquer. The reason is that the production of the elongated ellipsoid core by the commonly used alloys is technologically demanding. The way to deal with this problem is to use 3D printing technology. Nowadays there are several thermoplastic filaments which contains defined amount of a ferromagnetic addiction, but their magnetic properties are not well known.

2. METHODS AND RESULTS

For mutual comparison, the two types of cores have been designed. The first one has been designed in the shape of right cylinder as the most common core shape used in the magnetorquers applications. The second one is in the shape of prolate rotational ellipsoid. The body of this kind of shape has in its longitudinal direction the lowest demagnetization factor among all ellipsoidal bodies, which is suitable for the magnetorquers core application due their lower mass and power consumption. The demagnetizing factors of cores were calculated according to their geometric properties using interpolating formulas for the central demagnetization coefficient estimation [1].

Table 1. Parameters of ellipsoidal and cylindrical shaped cores

Parameter	Ellipsoidal shaped core	Cylindrically shaped core
Length L [m]	0,070	0,040 m
Diameter D [m]	0,005	0,080 m
Volume V [m^3]	$1{,}806 \cdot 10^{-6}$	$2{,}010 \cdot 10^{-6}$
Demagnetization factor N_d [-]	0,004	0,015

Based on the parameters from table 1., both cores were designed in CAD software and consequently printed by three-dimensional printer-Prusa i3 MK3S. To obtain the best magnetic properties a magnetically detectable filament was used.

2.1 Measurement of magnetic characteristics

The main goal of the measurement was to obtain hysteresis model of the printed samples. For this purpose, the stray magnetic field of the magnetized samples was measured. Both cores were magnetized in their longitudinal direction by the time-varying magnetic field generated by solenoid. The measurements and calculations were performed automatically by four channel magnetometer VEMA-04 [2].

According to the measurements results there are not expected hysteresis loops typical for ferromagnetic cores. From Fig 2. it is obvious that measured characteristic of the ellipsoidal shaped

sample has patterns of magnetic material so the most magnetic properties can be determined. However, its behavior is not acceptable for magnetorquers application mainly due to small values of magnetization.

In case of cylindrical shaped sample, the measured values of magnetization are in comparison with ellipsoidal shaped sample smaller by three orders, therefore the whole characteristic is way more affected by the ambient noise (see Fig 2.).

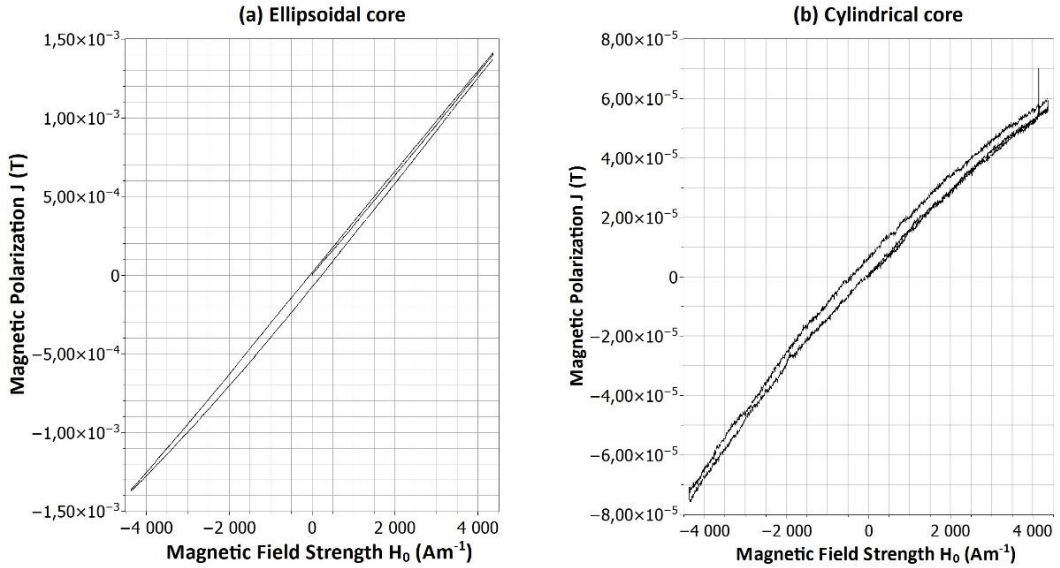

Figure 1 Magnetic Polarization vs Magnetic field Strength for ellipsoidal (a) and cylindrical core (b)

3. CONCLUSION

The unacceptable behavior of the used materials may be caused by a significant disproportion between the thermoplastic polymer and the ferromagnetic particles, which are randomly distributed in the volume of both samples. In that case the ferromagnetic particles are magnetized independently of each other hence it is not possible to measure the magnetization of the whole sample, only the combination of individual magnetic moments of these individual ferromagnetic particles and their concentrated clusters can be measured. It needs to be considered that these particles are mostly spherical in shape. Since demagnetization factor of the sphere is $N_S = 1/3$ there must be significant reduction of the total magnetic field.

For the sake of completeness, it should be mentioned that there is also noticeable contribution of the demagnetization field given by the geometrical properties of the whole bodies.

ACKNOWLEDGMENT

This research was funded by the Slovak Research and Development Agency, grant number APVV-17-0184 and grant number APVV-18-0248 and the Research Agency, ITMS code number 313011T557.

REFERENCES

[1] Sandomirsky, S.G.,: 2010, Simple and precise interpolating formulas for calculating the central demagnetization coefficient for ferromagnetic bodies, 10th European Conference on Non-Destructive Testing, Moscow (ECNDT). URL: https://www.ndt.net/search/docs.php3?id=9020

[2] Hudák, J., Blažek, J., Praslička, D., Mikita, I., Lipovský, P., Gonda, P.,: 2010, Sensitivity of VEMA-04.1 magnetometer, Journal of Electrical Engineering, Vol. 61, Issue 7/s, p. 28 – 31, 2010. ISSN 1335-3632

GUNSHOT DETECTION AND CLASSIFICATION

Opočenský, Michal[1]

[1]Department of Measurement, Faculty of Electrical Engineering of the Czech Technical University, Technická 2, 16627 Prague 6, Czech Republic
opocemi2@fel.cvut

1. INTRODUCTION

This article describes the gunshot detection algorithm and proposes gunshot classification algorithm. The gunshot is processed first by detection algorithm, which filters out non-gunshot events. Afterwards, the features are extracted by Mel-Frequency Cepstral Coefficients. The feature vector is then passed to the gunshot classification, performed through Support Vector Machine.

2. METHODS AND RESULTS

The detection and classification algorithms are described in this Section. Both were tested in Matlab for easier development.

2.1 Detection Algorithm

The detection algorithm [1] uses the time domain. It is working on the basis of the median filter, shown in Figure 1 for the noise extraction. The input signal is divided into taps, where the size

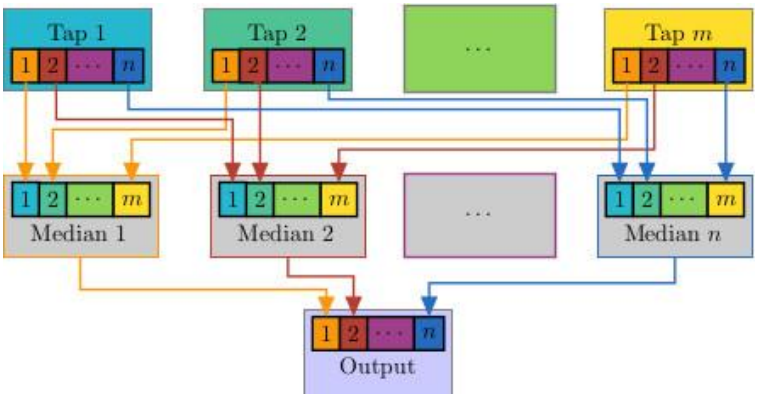

Figure 1. Visual median filter representation.

and number of taps are hyperparameters of the algorithm. Furthermore, the algorithm detects gunshots based on three parameters: audio level, energy, and Root Mean Square (RMS).

The algorithm approximates the background noise and then subtracts is from the middle tap, which should contain the main event (rising edge) of a potential gunshot. The gunshot is detected from the parameters based on two criterions. There are 2 values, that are used in the first gunshot criterion. The maximal value is determined from the newly created tap, and the RMS is calculated from the background noise. The second criterion is based on the median values of newly created taps around the maximal value, which is before and after the main rising edge of a potential gunshot.

In this particular case, the number of False Negative (FN) shall be zero, because FN means that a gunshot happened, but the algorithm did not recognize it as such.

Table 1. Detection algorithm confusion matrix

	Positive	**Negative**
True	169	52
False	95	5

2.2 Classification Algorithm

Classification of the acoustic event can potentially filter out more false-positive events that the detection algorithm (Section~\ref{subsec:det}). It also offers additional information about

possible incidents, mainly the classification of the gun caliber. For the classification, Mel-Frequency Cepstral Coefficients (MFCC) are used as the feature extractor, and afterwards the multiclass Support Vector Machine (SVM) classification is applied. The flowchart of classification is shown in Figure 3.

The used multiclass SVM classifier is one-to-all, which works by separating one class from all remaining classes. Determining to which class a given element belongs requires *n* classifications in the worst case, where *n* is the number of classes.

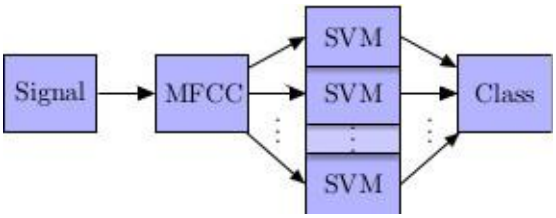

Figure 2. Classification flowchart.

Mel-Frequency Cepstral Coefficients (MFCC) are widely used in audio processing, especially for recognition of speech recording or song genre classification. The flowchart of retrieving the coefficients is in Figure 3. The whole algorithm has three parameters given by MFCC extraction: feature count, maximal frequency, and minimal frequency of mel-frequency filter bank.

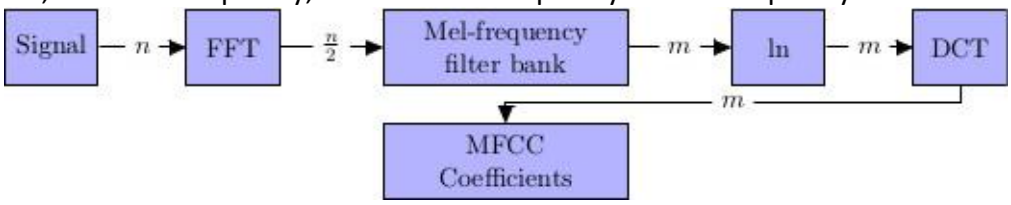

Figure 3. MFCC flowchart.

The loss of different classes is in Table 2. For example, the .22 LR subsonic has the highest cross-validation loss, most likely caused by the impact of the bullet in the shooting range, which is noticeable in comparison to other gunshot recordings.

Table 2. Classification algorithm error over 10-folds cross-validation.

Class	Loss
.22 LR	0.61 %
.22 LR subsonic	11.04 %
9 mm Luger	3.68 %
7.65 mm Browning	3.07 %
Mean	**4.60 %**

3. CONCLUSION

The detection algorithm based on paper [1] was tested on the provided dataset [2] with successful results.

Moreover, the classification algorithm, which determines the gunshot caliber with SVM classifier and MFCC feature extraction, shows excellent results of mean loss over classes for 10 folds cross-validation 4.6 % shown in Table 2, although the dataset provided for this purpose was limited.

REFERENCES

[1] J. Svatos and J. Holub, "Smart Acoustic Sensor.," *5th International Forum on Research and Technologies for Society and Industry: Innovation to Shape the Future, RTSI 2019 - Proceedings,* p. 61–165, 2019.

[2] J. Svatos and J. Holub, "Acoustic events dataset," 2019.

DTW-BASED STEP DETECTION ALGORITHM FOR PEDESTRIAN DEAD RECKONING

Oravec, M.[1]

[1]FEE CTU in Prague
oravemat@fel.cvut.cz

1. INTRODUCTION

In this talk, an algorithm of step detection to be used in a pederstian dead reckoning (PDR) positioning system (PS) is presented. It is primarily focused on smartphone-based PDR, but it is suitable also for other low-cost IMU (inertial measurement unit) based PDR implementations. The algorithm assumes the user has his smartphone placed in his pocket and it employs a dynamic time warping (DTW) technique to make the step detection less error-prone and much more universal.

The boom of smartphones in recent decades arranged for availability of a device with various sensors, high computational power, and an opportunity to communicate with external infrastructure in a pocket of nearly everyone. Combined with a strong need for accurate, reliable and easy-to-implement PS capable to operate not only outdoors but also indoors, it has opened smartphone-based positioning as a separate discipline.

Smartphones are typically equipped with plenty of sensors: IMU, a set of radio transceivers (Wi-Fi, LTE etc.), an infrared sensor etc. An usual smartphone-based PS combines a dead reckoning (DR) technique with radio-based positioning. Within their fusion, DR supports the radio-based location estimate and vice versa. Accuracy and robustness of each of the complementary systems plays an important role in performance of the final setup.

When talking about DR, the low-cost MEMS (micro electromechanical system) IMUs used in present smartphones do not generally allow for direct DR based on double integration of acceleration and single integration of rotation rate. Both the MEMS accelerometer and gyroscope are typically loaded with significant biases which make the position estimate unacceptably inaccurate after even a very short time. Instead, a group of PDR (pedestrian DR) algorithms is used. From IMU signals, PDR algorithms detect time instances when a user made a step, they estimate the step length, and from gyroscope and magnetometer data they find the user's heading.

2. METHODS AND RESULTS

The purpose of the proposed algorithm is to identify time instances when the user makes a bistep (a step by a right foot followed by a step by a left foot) while the smartphone is put in the user's right trouser pocket. To identify a bistep, one could use any of the sensor outputs provided by the smartphone. In our work, we take an advantage of Android smartphones. Using a custom application, we retrieve outputs of linear acceleration excluding gravity **a**, and rotation quaternion q describing the rotation from the IMU's body frame to an elevated local tangent plane ENU (east, north, up) frame sharing the same origin.

The algorithm works with vertical and horizontal acceleration (a_v and a_h, respectively) of the user's body. We use a simplification that the vertical axis of the user is aligned with the u axis of the ENU frame and the horizontal axis lies in the ENU frame's en-plane. After the coordinate conversion, both the a_h and a_v signals enter a cascade of lowpass filters to remove jitter noise. Once the a_v signal is preprocessed, one could observe a typical pattern in it, as could be seen in

Fig. 1a. Depending on walking pace the bistep image in the signal is compressed or prolonged in time and amplified or weakened. No matter what the actual pace is, we need to detect all the signal sections **y** which are similar to the bistep pattern (we will refer to it as **x**) from Fig. 1a.

The similarity between **x** and **y** is evaluated using the dynamic time warping (DTW) distance criterion. DTW is a method of finding the best alignment of two discrete sequences using their both local and global time compression or extension [1]. From an input of the two sequences **x** and **y**, it calculates the index sequences $\mathbf{i}_x$ and $\mathbf{i}_y$ such that sequences $\mathbf{x}[\mathbf{i}_x]$ and $\mathbf{y}[\mathbf{i}_y]$ have their mutual distance (DTW distance) *d* minimum along all possible $\mathbf{i}_x$ and $\mathbf{i}_y$. Detection of features in acceleration signal with DTW has been successfully used in [2]. Nonetheless, the method from [2] does not allow for significant changes in magnitude of pattern sections in the signal. In our algorithm both the input sequences are first normalized to unit RMS. The DTW distance corresponding to each sample of acceleration in *up* direction a_u is then taken as a minimum along multiple lengths of **y**. By adding the second dimension – time elapsed from the first sample – to the input sequences, we penalize big duration differences between **x** and **y**.

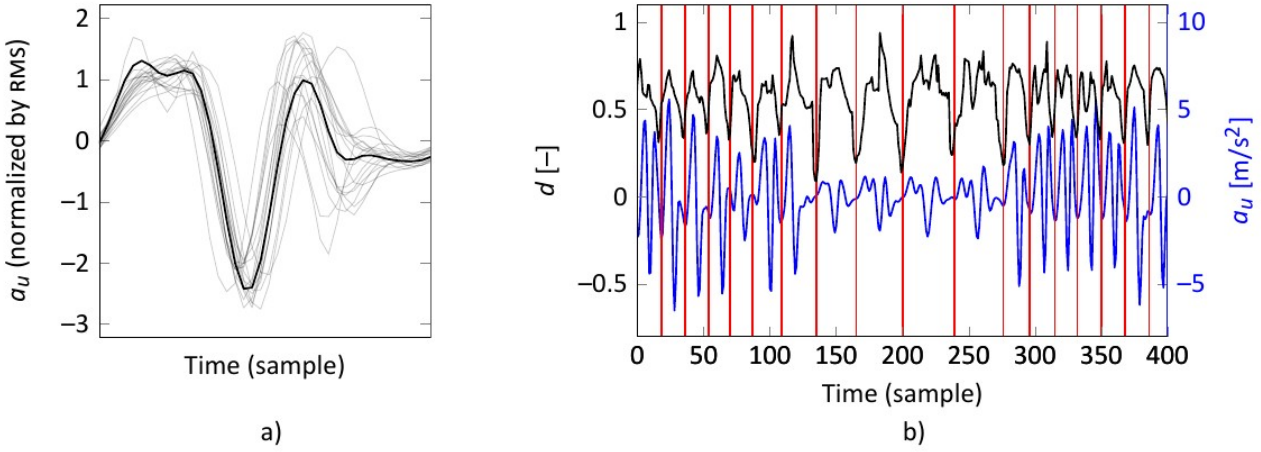

Fig. 1: Some of recorded bistep patterns and their mean value normalized by RMS (a) . Step instances (red vertical lines) detected by our algorithm (b).

3. CONCLUSION

As could be seen in Fig. 1b, detecting negative peaks of DTW distance could be done using a fixed threshold, opposite to detecting those in strongly dynamic course of vertical acceleration a_u. The algorithm successfully detects bisteps in a_u signal of varying-pace walk. Use of DTW makes the evaluation straightforward and it effectively liberate it from a complicated thresholding schemes needed in most of the contemporary step detection methods.

ACKNOWLEDGMENT

This work has been supported by the Technology Agency of the Czech Republic, grant No. TH03010261 and by the Czech Technical University in Prague, grant No. SGS20/129/OHK3/2T/13.

REFERENCES

[1] GIORGINO, T. (2009). "Computing and Visualizing Dynamic Time Warping Alignments in R: The dtw Package." *Journal of Statistical Software*, 31(7), 1–24. doi: 10.18637/jss.v031.i07.

[2] PERNEK, I and HUMMEL, K. and KOKOL, P. (2013). "Exercise repetition detection for resistance training based on smartphones." *Personal and Ubiquitous Computing*. 17. doi: 10.1007/s00779-012-0626-y.

SOFTWARE DEFINED INSTRUMENT DESIGNED FOR MASS DISTANCE LEARNING

Jakub Pařez

Czech Technical University in Prague, Faculty of Electrical Engineering
parezjak@fel.cvut.cz

1. INTRODUCTION

The key part of teaching electronics are practical experiments, where multiple laboratory measuring instruments are used. However, options for practical tasks are now significantly limited due to the worldwide coronavirus pandemic. Therefore, a solution that would help students to replace some of missing instruments would be useful.

It turns out, that this can be done with a powerful microcontroller, which can be purchased in the form of a cheap development kit, e.g. the Blue Pill with STM32F103C8. Moreover, this software defined instrument can be also used for mass parallel teaching at high schools or universities.

2. METHODS AND RESULTS

A typical instrument required for experiment is an oscilloscope, voltmeter and generator. The basic functionality of these devices can be implemented only using the internal blocks of MCU.

On Figure 1 is shown a block diagram of the resulting implementation of such a software defined instrument. Oscilloscope and voltmeter use ADC peripheral, logic analyzer uses GPIO peripheral, counter and a PWM generator are implemented by timer and a signal generator uses DAC. Wherever possible, DMA peripheral is used for fast data transfer. Communication with PC is realized with UART or USB peripherals, where USB is significantly faster.

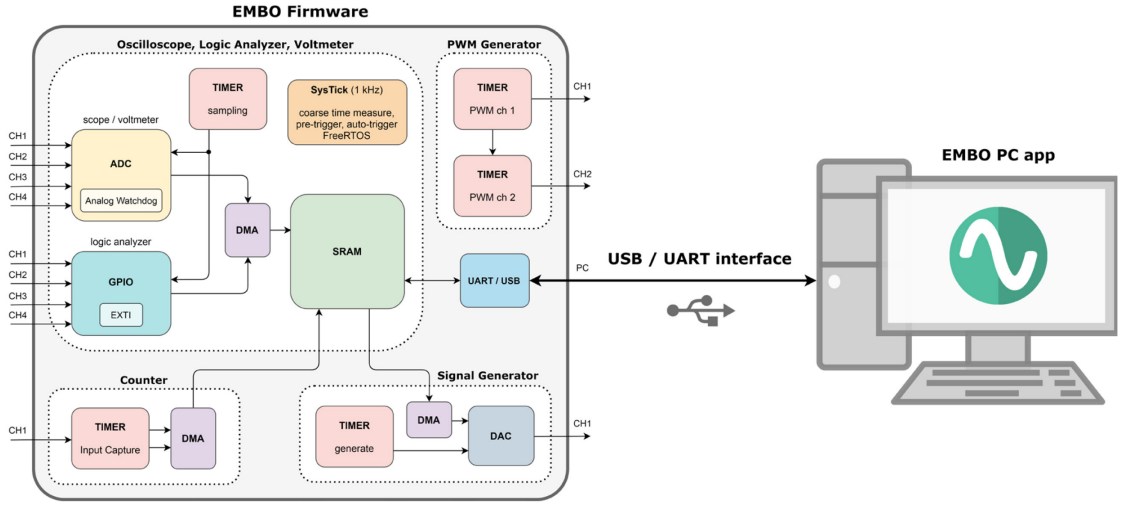

Figure 1. Block diagram of EMBO oscilloscope with focus on MCU peripherals and communication interface.

However, such a simple oscilloscope with ADC without buffer, which is connected directly to the circuit, has some limitations. Input range is limited to unipolar voltage 0-3.3 V and ADC inputs are not protected. Furthermore, maximum allowed impedance of signal source must not be exceeded. For STM32F103C8 at the shortest sampling time it is 73.4 Ω (Eq. 1). Parameters of the equation are sampling time $k = 1.5$, $f_{ADC} = 12$ MHz, $C_{ADC} = 8$ pF, $R_{ADC} = 1$ kΩ, $N = 12$ bit. [1]

$$R_{AIN-F103} \leq \frac{k - 0.5}{f_{ADC} \cdot C_{ADC} \cdot ln(2^{N+2})} - R_{ADC} \leq 73.4\ \Omega \quad (1)$$

Oscilloscope EMBO includes these instruments:

- Oscilloscope - 4 channel, 12/8 bit, FFT, averaging, cursors, data export (shown in Figure 2)
- Logic Analyzer - 4 channel, cursors, data export
- Voltmeter - 4 channel, chart recorder, averaging, cursors, data record
- Counter - 1 channel, slow/fast mode
- PWM Generator - 2 sync. channels
- Signal Generator - 1 channel, constant, sine, triangle, sawtooth, square, noise

Table 1. Main parameters and limits of EMBO oscilloscope instruments: oscilloscope (SCOPE), logic analyzer (LA), counter (CNTR), PWM generator (PWM), signal generator (SGEN). Maximum memory depth is labeled as DAQ.

MCU	PRODUCT	DAQ	ADC	SCOPE	LA	CNTR	PWM	SGEN
STM32F103C8	Blue Pill	10 kB	4 ch / 1 ADC	0.8 MSps	5.1 Msps	33 MHz	14.4 MHz	×
STM32F103RE	LQFP64	50 kB	4 ch / 2 ADC	0.8 MSps	5.1 Msps	33 MHz	14.4 MHz	4.5 MSps
STM32F303RE	Nucleo64	50 kB	4 ch / 4 ADC	4.9 Msps	14.4 Msps	57 MHz	20.6 MHz	4.5 MSps
STM32L412KB	Nucleo32	28 kB	4 ch / 2 ADC	5.0 Msps	13.3 Msps	37 MHz	16.0 MHz	×

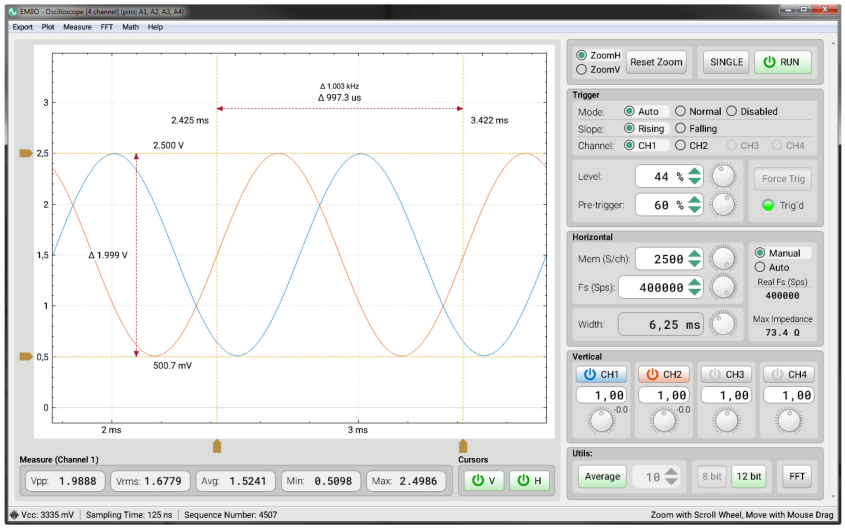

Figure 2. Main oscilloscope window (STM32F103C8). Input signals are two sine waves with frequency 1 kHz, phase shift 120° and amplitude 2 V. Sampling frequency is 400 kSps and memory depth 2500 samples per channel.

3. CONCLUSION

The result of my work is the EMBO (EMBedded Oscilloscope), which includes 3 primary instruments (oscilloscope, logic analyzer, voltmeter) and 3 secondary instruments (counter, PWM and signal generator). Multiplatform PC application written in C++ Qt is compiled for Windows, Ubuntu and macOS operating systems. Tested firmware written in C is available for STM32F103C8, STM32F103RE, STMF32F303RE and STM32L412KB in HEX format.

For the cheap Blue Pill board, the EMBO reaches a sampling frequency 800 kSps with total memory 10 kB. For the more expensive Nucleo-64 board, these values are much higher, the maximum sampling frequency is 4.965 MSps per channel with total memory 50 kB (limits shown in Table 1). For faster signals above the Nyquist frequency, such as op-amp response, equivalent-time sampling can be used, if the signal source is stable and periodic.

The EMBO oscilloscope will be used as a cheap and accessible tool in mass teaching, right from the next semester at CTU FEE.

REFERENCES

[1] ST Microelectronics, 2017, Reference manual for STM32F101xx, STM32F102xx, STM32F103xx, STM32F105xx andSTM32F107xx. Available at: https://www.st.com/

INKJET PRINTED PASSIVE COMPONENTS

Povolný, Vojtěch[1]

[1]Dept. of Microelectronics, Czech Technical University, Technická 2, 166 27 Praha, Czech
povolvoj@fel.cvut.cz

1. INTRODUCTION

Passive components like resistor, capacitor and inductor are basic stones of electrical circuits. Development of these components has come a long way which means that today we can reach very precise values. Inkjet printing is an alternative method how to fabricate electrical components. Inkjet printing has become more popular in recent few years thanks to fast process of fabricating from layout preparation to final product and with effective usage of material it is more efficient and ecological method of fabrication of samples. [1][2]

2. METHODS AND RESULTS

For inkjet printing are used many types of inks with a basic division to conductive, dielectric, semi conductive or magnetic. In this article there are used conductive and dielectric inks to prepare passive components on flexible substrate.

2.1 Substrate preparation

Samples were printed on PET foil Mitsubishi Novele™ IJ-220 which is flexible transparent substrate for low temperature preparation of printed structures. Surface of the substrate is pretreated and has modification which gives it good adhesion, accelerate drying and prevent from the flowing of the ink. This production modification makes this substrate ideal for inkjet printing.

2.2 Printing

The inks (silver nano-dispersion from Sigma-Aldrich PN-736465, carbon ink from Novacentrix PN 910-0145-02 and dielectric inks Dycotec materials DM-INI-7003 from Dycotec and XP PriElex SU-8 polymer material from Microchem) were printed with the inkjet material printer Fujifilm Dimatix DMP-2831. Platen temperature was set to 40 °C for silver and carbon ink and to 50 °C for dielectric inks and the cartridge to 35 °C for all inks. The drop spacing was set to 25 µm (1016 dpi), jetting frequency 2 kHz, jetting speed 11 m/s. Curing of the silver and carbon ink was performed by intense pulse light system Xenon X-1100 with conditions of 200 J and 200 µs what was experimentally proved as ideal settings. For curing of the dielectric ink was used UV LED diode with 380 nm and 1700 $mW \cdot cm^{-2}$. Measurement was performed with RLC meter Hameg 8118.

2.3 Resistors

Resistors were printed with carbon ink in 4 layers. Printed samples of the fabricated resistors can be seen in Figure 1. The length of each resistor is 10 mm and width are 100 µm, 200 µm and 300 µm respectively. Values of measured resistances can be seen in Table 1.

Table. 1 Parameters of printed capacitors

	A	B	C
LENGTH (mm)	10	10	10
WIDTH (µm)	100	200	300
RESISTANCE (kΩ)	170	93	60

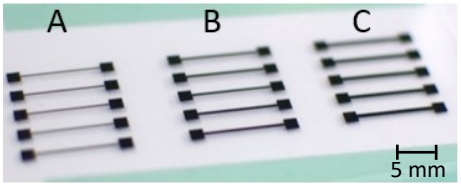

Figure 1. Resistors printed with carbon ink with different width; A) 100 µm, B) 200 µm, C) 300 µm

2.4 Capacitors

Capacitors were fabricated with silver and dielectric ink SU-8. Firstly, bottom electrode is printed with two layers of the silver ink and sintered. Printing of the dielectric ink follow as next layer. Dielectric is printed with 2 layers and each layer is cured for 2 min immediately after printing. Last step is to print top electrode with silver ink in 1 layer. The area of the capacitor is 9 mm^2. Measured capacitance of samples was 22 pF. Printed samples can be seen in Figure 2.

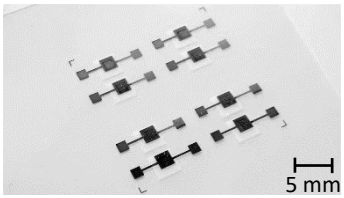

Figure 2. All inkjet printed capacitors printed with silver and dielectric ink

2.5 Inductors

Inductors were fabricated with silver and Dycotec dielectric ink. As a first step main part of the inductors with 5 thread and 150 µm wide line were printed with silver ink with 2 layers and sintered. Then, 4 mm wide stripe between the centers of the inductors was printed with dielectric ink and cured. On this stripe was then printed silver ink again to connect center electrodes of the inductors. Measured values of the inductance was 1 µH. Printed samples can be seen on Figure 3.

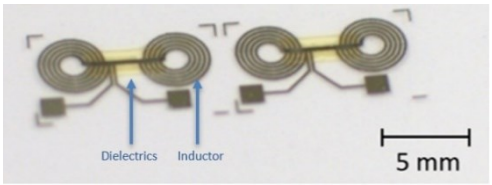

Figure 3. All inkjet printed inductors printed with silver and dielectric ink

3. CONCLUSION

I established printing process for fabrication of printed passive components. Each samples were subsequently characterized in terms of electrical properties, stability and repeatability. It was observed that carbon ink has approximately 10 000x higher resistivity than silver ink and therefore is suitable for printing resistive paths. Then were studied combination of conductive and dielectric inks. There were obtained that SU-8 ink has good dielectric properties for printing plate capacitors and Dycotec ink is suitable for printing insulation and passivation layers. The results are still preliminary and further research will be continued.

ACKNOWLEDGMENT

This work is part of the CTU SGS grant no. SGS20/176/OHK3/3T/13 and was supervised by Ing. Alexandr Laposa, Ph.D and Prof. Miroslav Husák (FEE CTU in Prague). Author wish to thank Assoc.prof. Jan Voves (FEE CTU in Prague) for advices.

REFERENCES

[1] B. J. Kang, C. K. Lee, and J. H. Oh, “All-inkjet-printed electrical components and circuit fabrication on a plastic substrate,” Microelectron. Eng., 2012, doi: 10.1016/j.mee.2012.03.032.

[2] V. Correia, K. Y. Mitra, H. Castro, J. G. Rocha, E. Sowade, and R. R. Baumann, “Design and fabrication of multilayer inkjet-printed passive components for printed electronics circuit development,” J. Manuf. Process., vol. 31, pp. 364–371, 2018, doi: 10.1016/j.jmapro.2017.11.016.

Practical aspects of an HTS SQUID operating as a geomagnetic sensor

Saunderson, EF[1,2], Dressler, M[3], Janosek, M[3]

[1]SANSA Space Science, Hermanus, South Africa
[2]Stellenbosch University, Stellenbosch, South Africa
[3]Czech Technical University in Prague, Prague, Czech Republic
esaunderson@sansa.org.za

1. INTRODUCTION

A commercial HTS SQUID (High-Temperature Superconductor Superconducting Quantum Interference Device) system is currently installed at SANSA Space Science in Hermanus, South Africa. It is operating unshielded as a geomagnetic sensor in an aluminium dewar using liquid Nitrogen cooling. The aim of our group from South Africa, France and Czech Republic is to explore the shortfalls and improve the field operation of the SQUID (data acquisition, system refilling etc.).

2. METHODS AND RESULTS

SQUID magnetometry started at SANSA Space Science through a collaborative project with LSBB in France since 2013 [1, 2]. The original focus was on the detection of magnetic seismic precursors, now we shifted to low-noise geomagnetic measurements for space weather observations [3]. The electronics and data acquisition were upgraded with CTU in Prague [4] and a new SQUID of own design is sought to be manufactured in France [5].

2.1 Improved HTS SQUID system at SANSA Space Science

Two M2700 HTS SQUIDs (noise <300 fT/√Hz) from StarCryo are currently installed, in H and Z orientation (Z currently operational) (Fig. 1-left). We are now upgrading the SQUIDs with 2 units from Forschungszentrum Juelich with a field noise <65 fT/√Hz, to have complete 3 axes. The SQUIDs are controlled with Magnicon SEL-1 electronics, and output is digitized at 12.5 Hz with a JANASCARD 24-bit integrating ADC and LabView software (Fig. 3), which will be supplemented with a National Instruments card to sample at 20 kHz soon. Before the SQUID was moved to a new location, it suffered from "flux-jumps" (Fig. 3) - additive quantization of the flux trapped in the SQUID ring, mainly due to RF disturbances. Currently the operation is fully stable in the new location, with jumps occurring only during LN_2 refills. The refilling of LN_2 into the dewar is a manual process, during which the temperature settling in the dewar affects the stability of the SQUID (Fig. 2). A new level measurement unit (Fig. 1-right) will allow refilling in one batch and minimize disturbances.

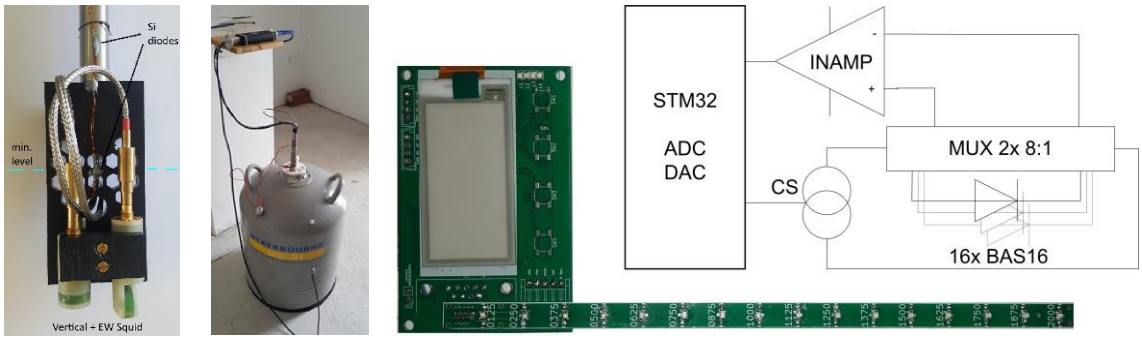

Figure 1. The SQUIDs (left) are housed in a 34l dewar (centre), new level measurement unit (right)

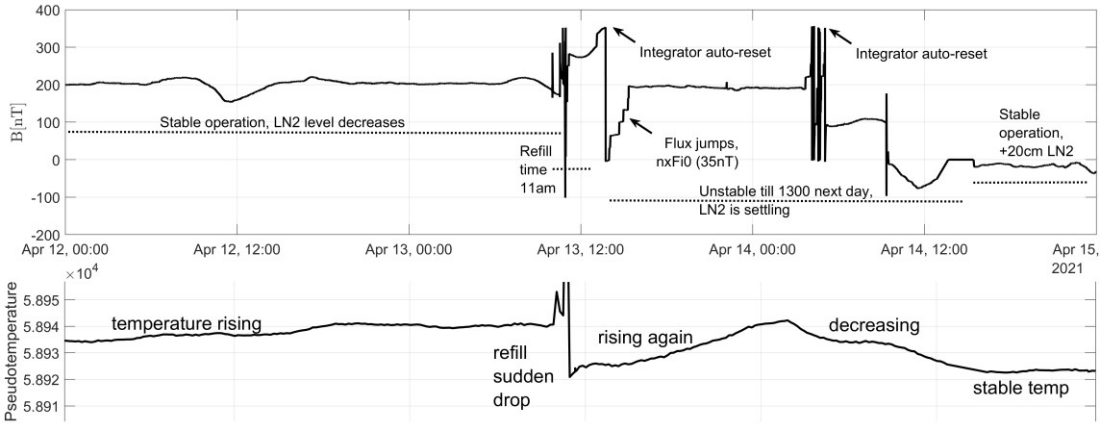

Figure 2. The SQUID output (top) and temperature variation of LN_2 (bottom) during LN_2 refilling process

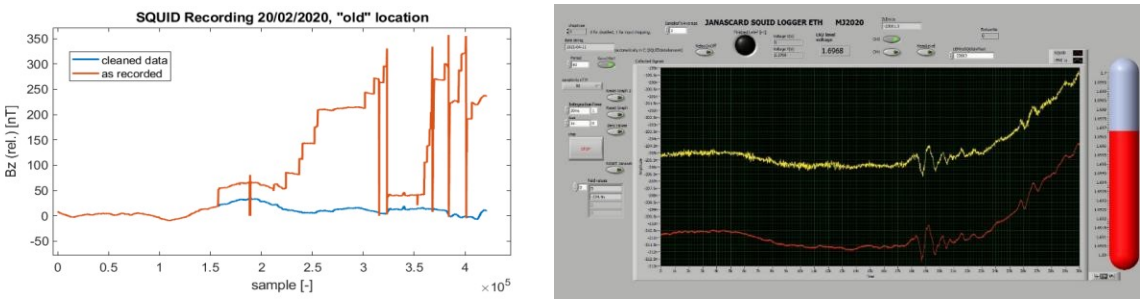

Figure 3. Flux jumps at the old location (left) and stable operation at the new location (right) - red trace is Z-axis SQUID and yellow trace is LEMI-025 fluxgate as reference

3. CONCLUSION

We present aspects of SQUID operating as a geomagnetic sensor (noise, stability, refilling) with the aim to widen the knowledge of usability of SQUIDs for that purpose. We show the importance of timely and non-disturbing LN_2 refills for continuous operation, which will be achieved with improved cryogenic LN_2 temperature/level measurement.

ACKNOWLEDGMENT

The authors acknowledge support of the IEEE Magnetics Society through the Educational Seed Funding 2021.

REFERENCES

[1] Fourie, C.J., et al, 2013, “First demonstration of transcontinental SQUID magnetometry”, AGU Fall Meeting, San Francisco, NH31B-1616.

[2] van Vuuren, Lucas J. Janse, et al., "Implementation of an unshielded SQUID as a geomagnetic sensor", 2013 Africon, IEEE, 2013.

[3] Matladi, T. et al, 2014, “Correlation between fluxgate and SQUID magnetometer data sets for geomagnetic storms”, in i-DUST 2014 , Apt, France.

[4] Janosek, M., Butta, M., Dressler, M., et al, 2019, “1 pT-noise fluxgate magnetometer design and its performance in geomagnetic measurements”, 2019 IEEE I2MTC.

[5] Janosek, M., Saunderson, E., Amari, P., et al, unpublished, “Design and testing of HTS DC SQUIDs manufactured using ion irradiation”, EUCAS 2019 conference, Glasgow.

HARDWARE PLATFORM FOR FRA AND FDS INSTRUMENTATION

Tomlain, J[1], Teren, O[1]

[1]Czech Technical University in Prague, Faculty of Electrical Engineering,
Department of Measurement
tomlajan@fel.cvut.cz

1. INTRODUCTION

In the field of energetics there is an amount of high-voltage (HV) machines those lifetime is expected of the order of tens of years. As an example the power transformers and generators directly used in the production and the transmission of electricity may be mentioned. To achieve the expected lifetime, it is necessary to plan regular diagnostic examinations of these machines, thus the machine operator avoids an unexpected shut down of the machine or the entire system [1]. There are a few measurements methods used to assess the state of the machine. This abstract further deals only with frequency response analysis (FRA) and frequency domain spectroscopy (FDS) which is a special case of dielectric spectroscopy. A brief description of the methods is stated. Similarities between these requirements are analysed in terms of common functional blocks of the instrumentation.

2. FRA AND FDS METHODS, HARDWARE PLATFORM AND RESULTS

The main idea behind the FRA process is to measure the transfer function of the inspected subsystem in some frequency span. The diagnostic result for the high voltage machinery FRA is a relationship between ac impedance of the device under test (DUT) as a function of the excitation voltage or current frequency [2]. It has been verified that even minor displacements in the geometric structure of the large power transformer windings or changes in the dielectric parameters of the insulation system will lead to the relevant changes in the FRA fingerprint.

The FDS is one of the methods suitable for studying the polarization phenomena. The FDS is a method that utilized an ac current excitation of studied material (transformer insulation). The capacitance and the dissipation factor are measured as a function of frequency of the excitation signal [3].

The common feature is the both methods utilize the measurement of electrical impedance with respect to excitation current frequency. Only the interpretation is slightly different. These similarities led authors to explore possibilities of development of a measuring platform implementing both methods. The platform would form a core of one single instrument able to execute both FRA and FDS measurements without any measurement precision degradation. A block diagram of the proposed instrument platform is shown in Figure 1. A field-programmable gate array (FPGA) core acts as a control unit of the platform. It drives a signal generator using direct digital synthesis (DDS) algorithm. The algorithm is able to generate an arbitrary waveform. An optional high voltage amplifier can be used to amplify the output signal (especially when using FDS method). The platform is equipped with two vector ammeters. Each ammeter is able to detect the amplitude and phase (related to the excitation signal) of the measured current.

Testing procedure of the complete system took place in the laboratory environment as well as on the real DUT in form of the high-power distribution transformers. Based on the past simulations, a simple testing prototype was built. The reference measurement was done by the professional impedance analyser MFIA (Zurich Instruments). The frequency span from 1 Hz to 100

kHz was used for the laboratory tests. Accuracy of this instrument is typically 0.05 % in the selected working range. Errors plots are shown in Figure 2 a,b,c.

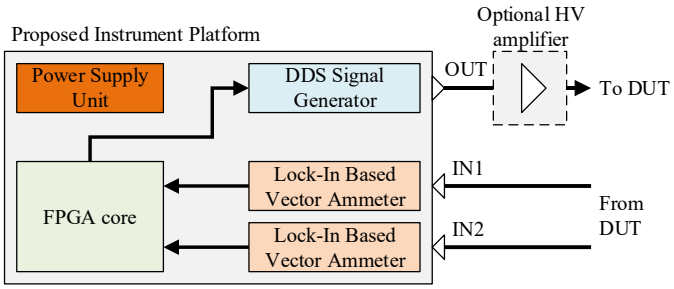

Figure 1. The block diagram of the proposed instrument platform.

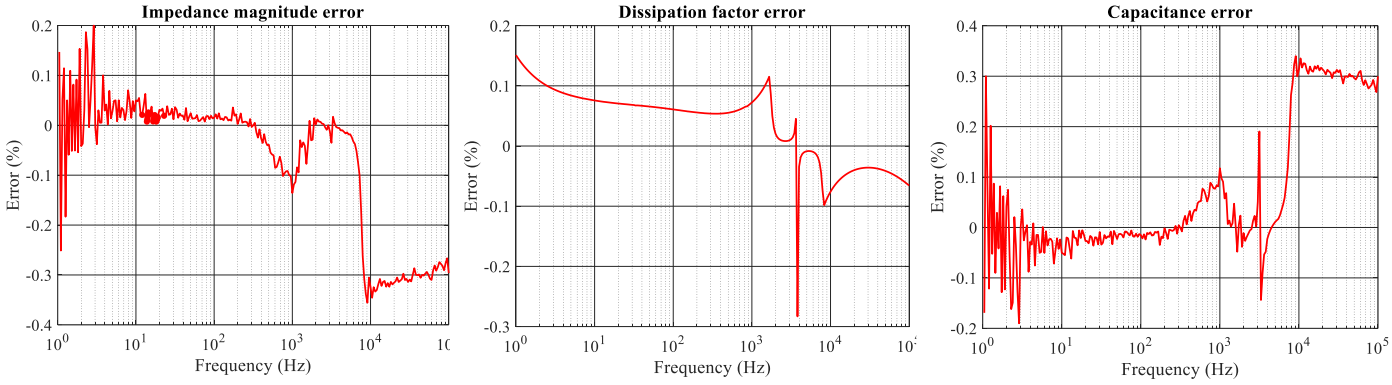

Figure 2. a, b, c Measurement errors of impedance magnitude, dissipation factor and capacitance.

3. CONCLUSION

This abstract deals with a non-invasive diagnostic of high voltage machines. Special emphasis is given to frequency response and frequency domain spectroscopy. The reference measurement of the testing circuit was executed by a laboratory instrument with precision 0.05 %. Then, the testing circuit was used to evaluate platform precision in a frequency range from 1 Hz up to 100 kHz. The evaluation experiments revealed that the relative error of impedance magnitude did not exceed 0.4 %, the relative error of dissipation factor 0.3 % and relative error of capacitance 0.4 %.

ACKNOWLEDGMENT

The project is held at the Department of Measurement, Faculty of Electrical Engineering, CTU in Prague under supervision of Assoc. Prof. Josef Vedral, CSc. and Radek Sedlacek, PhD and supported by the Grant Agency of the CTU in Prague under the grant No. SGS20/073/OHK3/1T/13.

REFERENCES

[1] Simons, J.,: 1980, Diagnostic testing of high-voltage machine insulation. A review of ten years' experience in the field, IEE Proceedings B - Electric Power Applications, vol. 127, no. 3, pp. 139–154,

[2] Abu-saida A., Hashemnia, N., Islam, S., Masoum, M. S. A.: 2012, Impact of transformer model parameters variation on FRA signature, Universities Power Engineering Conference (AUPEC), 2012 22nd Australasian, pp. 1–5,

[3] Abhishek, J., Aradhi, P.: 2012, Dielectric diagnosis of EHV current transformer using frequency domain spectroscopy (FDS) & polarization and depolarization current (PDC), International Journal of Scientific & Engineering Research, vol. 3.

Proceedings of Student Conference on Sensors, Systems and Measurement 2021

Published in 2021 by the Czech Technical University in Prague
Faculty of Electrical Engineering, Department of Measurement
Technická 2, 166 27, Prague 6, Czech Republic
First edition, 41 pages
ISBN 978-80-01-06822-9